Theoretical Methods for the Prediction of Near-Field and Far-Field Sound Radiation of Fan Tones Scattered By A Cylindrical Fuselage*

Dionysios-Marios Rouvas† and Alan McAlpine‡
Institute of Sound and Vibration Research, University of Southampton, Southampton, SO17 1BJ, United Kingdom

The aim of the work presented in this paper is the development of theoretical methods to predict scattering of fan tone noise from a turbofan engine by the airframe fuselage. The analysis begins with an overview of previous research on fan tone noise scattering by an adjacent cylindrical fuselage. In all similar previous work the propagation of sound through the fuselage boundary layer has been calculated using numerical methods. The effect of the boundary layer can be very significant on the upstream radiated sound from a turbofan's intake. An asymptotic approach is presented to model sound propagation within the boundary layer. An entirely analytic formulation is derived for a thin linear velocity profile. This approach leads to a far-field solution expressed in terms of a Fourier series, and a near-field solution expressed in terms of a Fourier series and a Fourier inverse transform. The new formulation is validated by comparison with simpler analytic solutions, and against existing numerical solutions. Furthermore, the results using a linear velocity profile are shown to be comparable with numerical results calculated with a realistic shear velocity profile that closely matches a turbulent boundary layer. Preliminary results from the new theoretical method are presented that illustrate the refraction effect by the fuselage boundary layer.

I. Nomenclature

a	=	duct radius, m
a_0	=	fuselage radius, m
B_n	=	Fourier coefficient for scattered field, uniform flow
b	=	distance between the centreline of the fuselage and centreline of the intake duct, m
C_n	=	Fourier coefficient for scattered field, flow with boundary layer
c_0	=	speed of sound, m·s^{-1}
E_n	=	Fourier coefficient for incident field, flow with boundary layer
$\mathrm{H}_m^{(2)}$	=	Hankel function of the second kind, order m
I	=	denotes integral
J_m	=	Bessel function of the first kind, order m
K	=	non-dimensional axial wavenumber
k_0	=	freespace wavenumber, rad·m^{-1}
k_{zlq}	=	axial wavenumber, mode (l, q), rad·m^{-1}
l	=	azimuthal order
M_0	=	free-stream Mach number
M_w	=	Mach number at the fuselage surface
P_{lq}	=	pressure amplitude of mode (l, q), Pa
p'	=	acoustic pressure, Pa

*This is the author's version (post-print) of the work that was accepted for publication in the proceedings of the AIAA Aviation 2021 Forum, August 2-6.

© 2021. This manuscript version is made available under the CC-BY-NC-ND 4.0 license; http://creativecommons.org/licenses/by-nc-nd/4.0/

The final version was published in the proceedings of the conference as paper No. 2021-2300. https://doi.org/10.2514/6.2021-2300

†PhD Candidate, Institute of Sound and Vibration Research (ISVR), D-M.Rouvas@soton.ac.uk.

‡Associate Professor, Institute of Sound and Vibration Research (ISVR), A.McAlpine@soton.ac.uk.

q = radial order
(r, ϕ, z) = cylindrical coordinate system centered on the intake duct (or disc source))
$(\bar{r}, \bar{\phi}, \bar{z})$ = cylindrical coordinate system centered on the fuselage
$(\bar{R}, \bar{\theta}, \bar{\phi})$ = spherical polar coordinate system centred on the fuselage
t = time,s
Γ = radial wavenumber, rad·m^{-1}
γ = alternative form of radial wavenumber, rad·m^{-1}
Δ_0 = wavenumber in real space used in far-field analysis, dependent on $\bar{\theta}$, rad·m^{-1}
Δ_{bl} = difference between sound pressure level with and without the presence of a boundary layer, dB
δ = boundary layer thickness, m
ϵ = non-dimensional error metric
ε = non-dimensional boundary layer thickness
ζ = non-dimensional radial coordinate used to denote location within the boundary layer
κ_{lq} = modal eigenvalue, mode (l, q), rad·m^{-1}
φ = Mach number distribution inside the boundary layer, dependent on ζ
ω_0 = angular frequency, rad·s^{-1}

Subscripts

ff = denotes far-field quantity
i = denotes incident field
in = denotes field inside the boundary layer
n = denotes quantity is a Fourier–Bessel harmonic
out = denotes field outside the boundary layer
s = denotes scattered field
t = denotes total field
0 = denotes free stream value

Superscripts

$'$ = denotes differentiation with respect to a function's argument

Symbol

$\widehat{\ }$ = denotes time-harmonic quantity
$\bar{\ }$ = denotes Fourier transformed quantity

II. Introduction

With the introduction of the turbojet engine in the 1950s, commercial aviation entered an era of unprecedented growth. Over the years, organisations around the world, for example the International Civil Aviation Organisation [1], have introduced rules and regulations that dictate certain standards regarding noise levels produced by commercial aircraft. The aim of these standards is to maintain low noise pollution levels despite the frequency of flights continuing to increase. It is clear that in order for the industry to meet these standards, the use of accurate noise prediction methods is required.

The most important noise sources can be categorised into three broad groups: engine noise; jet noise; and, airframe noise. The distribution, strength and directivity of these sources depend on the configuration of the aircraft. The engine position, engine model, fuselage and wing configuration are all factors to be taken into consideration when calculating the contribution of each source. Fan noise is one of the dominant sources both during take-off and approach [2]. However, previous researchers (for example Hanson [3], Hanson and Magliozzi [4], Fuller [5]) have cited that it is not sufficient to predict the propagation of fan noise in free space, since the engine will be adjacent to the fuselage or

other parts of the airframe. It is evident that the sound field will interact with the various parts of the airframe. These interactions are referred to as acoustic installation effects.

Since fan noise is one of the dominant sources, the work in this paper focuses on the modelling of fan tone radiation and its interaction with an adjacent aircraft fuselage. This interaction leads to substantial alterations in the acoustic field compared with the same source in free space. Alterations are expected both for the near and the far field. For that reason it is misleading to calculate only the free-field response of the noise source, its acoustic installation effects must be included. Installation effects are important for the aviation industry to understand and predict since community noise exposure, quantified in terms of the Effective Perceived Noise Level (EPNL) metric, is a function of the noise generated by the aircraft as a whole.

The aim of this work is the development of theoretical methods to predict scattering of fan tone noise from a turbofan engine by the airframe fuselage. Fan noise includes strong tonal components, thus the analysis is based on a time-harmonic sound field. More specifically, the aim is to develop and validate analytic expressions that describe the acoustic near- and far-field from an installed fan tone noise source adjacent to a cylindrical fuselage. This model shown illustrated in Fig. (1) replicates the real-life situation of a turbofan engine mounted under the wing with its intake duct next to the fuselage. In this work, the term scattering will refer to reflection and diffraction around a cylindrical fuselage. The fan tone noise source is modelled by a distributed disc source which simulates an acoustic spinning mode radiated from a cylindrical intake. The total field, comprised of the sum of the incident field and scattered field, is calculated separately for the near- or far-field. The objective is to provide physical insight of the acoustic field in the presence of the cylindrical fuselage, with the key application being fan tone radiation from ultra high-bypass-ratio turbofan engines.

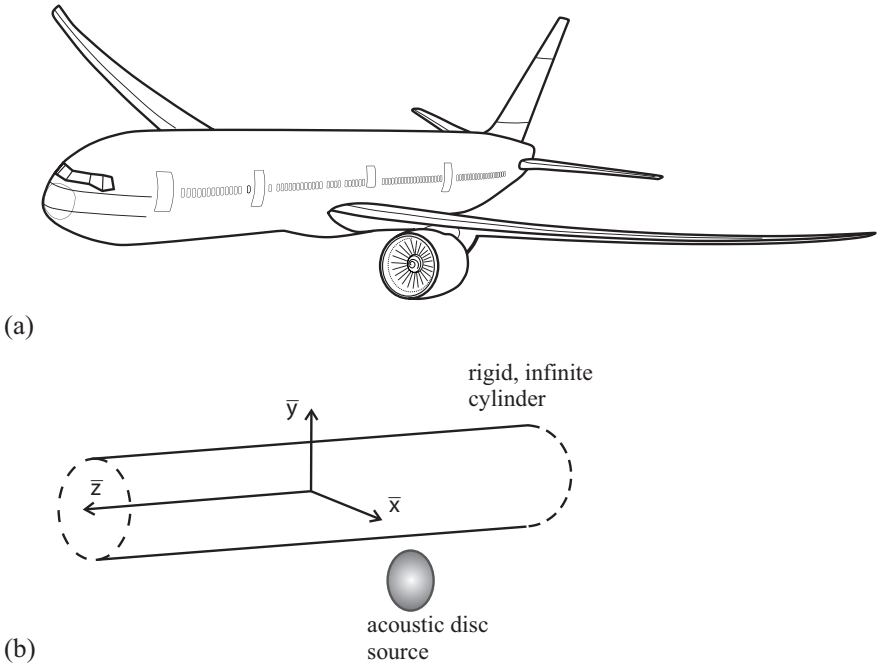

Fig. 1 Sketch of an installed turbofan aero-engine. Taken from Ref. [8].

The principal novel contributions of this work are the following. Previous work on the same topic has used numerical solutions (for example McAninch [6], Tam and Morris [7], Hanson and Magliozzi [4], McAlpine, Gaffney and Kingan [8], Gaffney, McAlpine and Kingan [10]), whereas in this article all the formulations are entirely based on analytical methods. Analytical solutions have extremely low computational cost, and in acoustics can be used to provide rapid predictions and physical insight of realistic noise problems. Secondly, this work focusses on both the acoustic far-field as well as the near-field. Most of the research so far has been restricted to the near-field pressure that affects cabin noise, with very few researchers (with the exception of Lu [11]) considering in detail the far-field that affects ground noise. In this paper, expressions are derived for the polar and azimuthal directivity around the fuselage. Thirdly, it is demonstrated that the predicted results from the analytic methods are comparable with other numerical methods, and that the simplifications involved in the theory do not compromise the accuracy of the results.

A large proportion of the research on fuselage scattering has focussed on the effect of the boundary layer on the

sound propagation. The objective is to predict the characteristic refraction of the upstream propagating sound due to the presence of a boundary layer on the fuselage as shown illustrated in Fig. (2). In the last forty years, methods have been proposed and successfully implemented to predict the acoustic pressure on the fuselage surface in the presence of a boundary layer. McAninch [6] was the first researcher to identify the difficulties associated with analytically solving the sound propagation in a shear layer. Several researchers after that focused on the scattering by the fuselage accounting for propagation of the sound through the fuselage's boundary layer. Hanson and Magliozzi [4] were the first to introduce a model for predicting the scattered field due to an adjacent propeller source. It was not until recently that a comparable model was introduced that predicted the scattering of fan tone sources by the fuselage (Gaffney et al. [10]). Furthermore, all the previous methods require a numerical evaluation of the Pridmore-Brown equation to predict the sound field contained within the boundary layer. In this paper, an analytic method is outlined to predict the sound field within the boundary layer, solving the Pridmore-Brown equation. This is based on an asymptotic method in duct acoustics by Eversman and Beckemeyer [12].

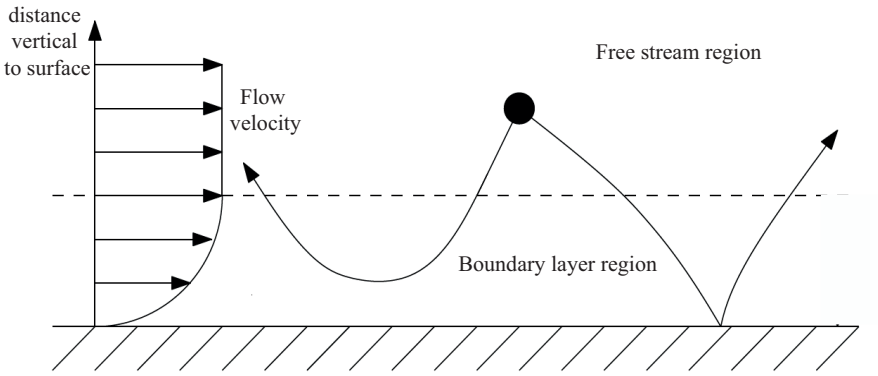

Fig. 2 Sketch of refracted rays downstream and upstream of the source. Taken from Ref. [14].

III. Theoretical Background and Analysis

A. In-duct Sound Field

Following McAlpine et al. [8], the analysis starts by considering a ducted fan in a cylindrical intake of radius a. The original cylindrical polar coordinate system that is used has its z-axis coincident with the centreline of the intake duct (as shown in Fig. (3)). Also there is a subsonic uniform mean flow, Mach number $M_z = U_z/c_0$, directed in the negative z-direction. The sound field generated by the ducted fan is modelled using "spinning modes" [15]. To avoid any confusion, it is stated that in the following analysis the time-harmonic convention is $\exp\{+\mathrm{i}\omega_0 t\}$. A time-harmonic spinning mode with azimuthal order l and radial order q has acoustic pressure and axial particle velocity given by (eqs.(1) through (4) in Ref. [8])

$$\hat{p}_{lq} = P_{lq}\mathrm{J}_l(\kappa_{lq}r)\mathrm{e}^{\mathrm{i}(-l\phi - k_{zlq}z)}, \tag{1}$$

$$\hat{u}_{zlq} = \frac{\xi_{lq}}{\rho_0 c_0} P_{lq}\mathrm{J}_l(\kappa_{lq}r)\mathrm{e}^{\mathrm{i}(-l\phi - k_{zlq}z)}, \tag{2}$$

where P_{lq} is the modal amplitude,

$$\xi_{lq} = \frac{k_{zlq}}{(k_0 + k_{zlq}M_z)}, \tag{3}$$

and the dispersion relationship is given by

$$k_{zlq}^2 + \kappa_{lq}^2 = (k_0 + k_{zlq}M_z)^2. \tag{4}$$

The Bessel function of the first kind and order l is denoted by J_l. Also, κ_{lq} is the set of eigenvalues which satisfy $\mathrm{J}_l'(\kappa_{lq}a) = 0$, k_{zlq} is the axial wavenumber of mode (l, q), c_0 is the speed of sound, ρ_0 is the mean density of the air inside the duct, and the freespace wavenumber $k_0 = \omega_0/c_0$. The cylindrical polar coordinates are (r, ϕ, z).

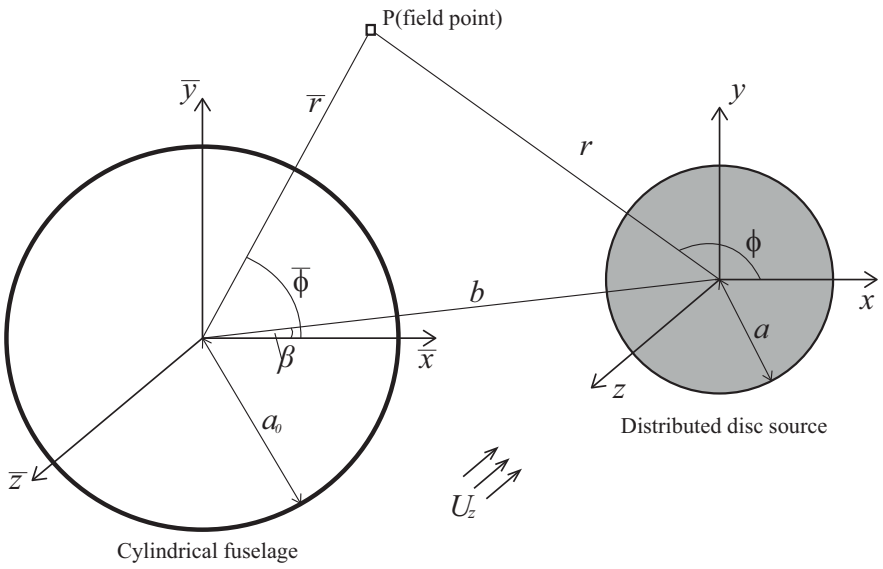

Fig. 3 Coordinate systems for the source and the cylinder.

B. Uniform Flow Analysis

From McAlpine et al. [8], the acoustic pressure generated by a fan tone exiting a cylindrical duct is modelled by integrating a distribution of monopole sources over the cross-section of the duct termination. In this paper only a brief review of the derivation is presented in the appendix; the full derivation is in Ref. [8]. The acoustic pressure is

$$p_i'(r,\phi,z,t) = \frac{\xi_{lq}P_{lq}}{4}\int_{-\infty}^{\infty}(k_0+k_zM_z)\Psi_{lq}\mathrm{H}_l^{(2)}(\Gamma_0 r)\mathrm{e}^{-\mathrm{i}k_z z}\mathrm{d}k_z\mathrm{e}^{-\mathrm{i}l\phi}\mathrm{e}^{\mathrm{i}\omega_0 t}. \tag{5}$$

This equation describes the incident field and it is in terms of the cylindrical coordinate system centered on the centerline of the source. However, the scattered field is centered on the fuselage, because the scattered waves take the form of the scattering surface. Thus the incident field needs to be shifted from the source's coordinate system to the fuselage's coordinate system. This is performed by using Graf's Addition Theorem listed in Abramowitz and Stegun [16], and detailed in the appendix.

An important distinction must be made here. In order to use Graf's theorem, in this paper the near-field is considered the space where $\bar{r} < b$, and the far-field is considered the space where $\bar{r} > b$. The geometrical parameters are shown in Fig.(3). For the near-field result where $\bar{r} < b$, the Fourier transformed incident pressure is dependent on $\bar{r}$ via a Bessel function

$$\overline{p_{in}'}(\bar{r},k_z,t) = \pi^2\xi_{lq}P_{lq}(-1)^{l+n}(k_0+k_zM)\,\Psi_{lq}\,\mathrm{e}^{-\mathrm{i}(l-n)\beta}\,\mathrm{H}_{l-n}^{(2)}(\Gamma_0 b)\,\mathrm{J}_n(\Gamma_0\bar{r})\,\mathrm{e}^{\mathrm{i}\omega_0 t}, \tag{6}$$

where $\Gamma_0^2 = (k_0+k_zM_z)^2 - k_z^2$ is a radial wavenumber and the function Ψ_{lq} is given by

$$\Psi_{lq} = \frac{\Gamma_0 a}{\kappa_{lq}^2-\Gamma_0^2}\mathrm{J}_l(\kappa_{lq}a)\mathrm{J}_l'(\Gamma_0 a), \quad \Gamma_0 \neq \kappa_{lq}, \tag{7}$$

$$\Psi_{lq} = \frac{1}{2}\left(a^2 - \frac{l^2}{\kappa_{lq}^2}\right)\mathrm{J}_l^2(\kappa_{lq}a), \quad \Gamma_0 = \kappa_{lq}. \tag{8}$$

McAlpine et al. [8] did not derive the far-field result. In this case, where $\bar{r} > b$, application of Graf's theorem will give a modified incident field dependent on $\bar{r}$ through a Hankel function (as first shown by Lu [11])

$$\overline{p_{in}'}(\bar{r},k_z,t) = \pi^2\xi_{lq}P_{lq}\,(k_0+k_zM)\,\Psi_{lq}\,\mathrm{e}^{\mathrm{i}(n-l)\beta}\,\mathrm{J}_{n-l}(\Gamma_0 b)\,\mathrm{H}_n^{(2)}(\Gamma_0\bar{r})\,\mathrm{e}^{\mathrm{i}\omega_0 t}. \tag{9}$$

The governing equation that describes the scattered field is the homogeneous convected wave equation, and since the solution must be outward propagating cylindrical waves it can be expressed in terms of a Hankel function,

$$\overline{p_{sn}'}(\bar{r},k_z,t) = \frac{1}{2\pi}B_n(k_z,\omega_0)\mathrm{H}_n^{(2)}(\Gamma_0\bar{r})\,\mathrm{e}^{\mathrm{i}\omega_0 t}. \tag{10}$$

By taking the total Fourier transformed pressure field given by the sum of the incident and the scattered fields,

$$\overline{p'_{tn}}\,(\bar{r},k_z,t) \;=\; \overline{p'_{in}}\,(\bar{r},k_z,t) \;+\; \overline{p'_{sn}}\,(\bar{r},k_z,t), \tag{11}$$

and by employing a rigid hard-wall boundary condition at the fuselage surface,

$$\frac{\partial\overline{p'_{tn}}}{\partial\bar{r}} = \frac{\partial\overline{p'_{in}}}{\partial\bar{r}} + \frac{\partial\overline{p'_{sn}}}{\partial\bar{r}} = 0 \quad \text{at} \quad \bar{r}=a_0, \tag{12}$$

where $\overline{p'_{in}}$ is the near-field expression given by eq.(6) since the fuselage surface lies in the near-field, one can solve for the coefficient $B_n(k_z,\omega_0)$,

$$B_n(k_z,\omega_0) \;=\; -2\pi^3\xi_{lq}P_{lq}(-1)^{l+n}\,\mathrm{e}^{-\mathrm{i}(l-n)\beta}\,(k_0+k_zM)\,\Psi_{lq}\,\mathrm{H}^{(2)}_{l-n}(\Gamma_0 b)\,\frac{\mathrm{J}'_n\,(\Gamma_0 a_0)}{\mathrm{H}^{(2)\prime}_n\,(\Gamma_0 a_0)}. \tag{13}$$

By substituting eq.(13) into eq.(10), the Fourier transformed scattered field is obtained,

$$\overline{p'_{sn}}\,(\bar{r},k_z,t) \;=\; -\pi^2\xi_{lq}P_{lq}(-1)^{l+n}\,\mathrm{e}^{-\mathrm{i}(l-n)\beta}\,(k_0+k_zM)\,\Psi_{lq}\,\mathrm{H}^{(2)}_{l-n}(\Gamma_0 b)\,\mathrm{H}^{(2)}_n\,(\Gamma_0\bar{r})\,\frac{\mathrm{J}'_n\,(\Gamma_0 a_0)}{\mathrm{H}^{(2)\prime}_n\,(\Gamma_0 a_0)}\,\mathrm{e}^{\mathrm{i}\omega_0 t}. \tag{14}$$

Finally the total field is found by summing the incident field and the scattered field, either in the near-field in which case equations (6) and (14) are summed together, or in the far-field in which case equations (9) and (14) are summed together. The total field in real space is found by performing an inverse Fourier z-transform

$$p'_t\,(\bar{r},\bar{\phi},\bar{z},t) \;=\; \frac{1}{(2\pi)^2}\sum_{n=-\infty}^{\infty}\int_{-\infty}^{\infty}\overline{p'_{tn}}\,(\bar{r},k_z,t)\,\mathrm{e}^{-\mathrm{i}k_z\bar{z}}\,\mathrm{d}k_z\,\mathrm{e}^{-\mathrm{i}n\bar{\phi}}. \tag{15}$$

1. Fuselage Surface Pressure

The near-field case is of interest on setting $\bar{r}=a_0$ since it describes the pressure on the fuselage surface. By setting $\bar{r}=a_0$ and using eq.(11) with the Fourier transformed incident field given by eq.(6) and scattered field given by eq.(14),

$$\begin{aligned}\overline{p'_{tn}}\,(a_0,k_z,t) \;=\;& \pi^2\xi_{lq}P_{lq}\,(-1)^{l+n}\,\mathrm{e}^{-\mathrm{i}(l-n)\beta}\,(k_0+k_zM)\,\Psi_{lq}\,\mathrm{H}^{(2)}_{l-n}\,(\Gamma_0 b)\times\\ &\left[\frac{\mathrm{J}_n\,(\Gamma_0 a_0)\mathrm{H}^{(2)\prime}_n\,(\Gamma_0 a_0)-\mathrm{J}'_n\,(\Gamma_0 a_0)\,\mathrm{H}^{(2)}_n\,(\Gamma_0 a_0)}{\mathrm{H}^{(2)\prime}_n\,(\Gamma_0 a_0)}\right]\mathrm{e}^{\mathrm{i}\omega_0 t}.\end{aligned} \tag{16}$$

Then by using the Wronskian formula,

$$\mathrm{J}_n\,(x)\,\mathrm{H}^{(2)\prime}_n\,(x)-\mathrm{J}'_n\,(x)\,\mathrm{H}^{(2)}_n\,(x) = -\mathrm{i}\left(\frac{2}{\pi x}\right), \tag{17}$$

the following is obtained,

$$\begin{aligned}\overline{p'_{tn}}\,(a_0,k_z,t) \;=\;& \pi^2\xi_{lq}P_{lq}\,(-1)^{l+n}\,\mathrm{e}^{-\mathrm{i}(l-n)\beta}\,(k_0+k_zM)\,\Psi_{lq}\,\mathrm{H}^{(2)}_{l-n}\,(\Gamma_0 b)\times\\ &\left[\Big(-\mathrm{i}(2/\pi\Gamma_0 a_0)\Big)/\mathrm{H}^{(2)\prime}_n\,(\Gamma_0 a_0)\right]\mathrm{e}^{\mathrm{i}\omega_0 t}.\end{aligned} \tag{18}$$

Finally, the total pressure in real space is given by eq.(15) substituting $\overline{p'_{tn}}\,(\bar{r},k_z,t)$ with $\overline{p'_{tn}}\,(a_0,k_z,t)$ from eq.(18),

$$p'_t\,(a_0,\bar{\phi},\bar{z},t) \;=\; \frac{\xi_{lq}P_{lq}}{4}\,(-1)^l\,\mathrm{e}^{-\mathrm{i}l\beta}\,\mathrm{e}^{\mathrm{i}\omega_0 t}\sum_{n=-\infty}^{\infty}\left\{(-1)^n\,I_n\,(a_0,\bar{z})\,\mathrm{e}^{-\mathrm{i}n(\bar{\phi}-\beta)}\right\}, \tag{19}$$

where

$$I_n\,(a_0,\bar{z}) \;=\; \int_{-\infty}^{\infty}(k_0+k_zM)\,\Psi_{lq}\,\mathrm{H}^{(2)}_{l-n}\,(\Gamma_0 b)\left[\Big(-\mathrm{i}(2/\pi\Gamma_0 a_0)\Big)/\mathrm{H}^{(2)\prime}_n\,(\Gamma_0 a_0)\right]\mathrm{e}^{-\mathrm{i}k_z\bar{z}}\,\mathrm{d}k_z. \tag{20}$$

This integral cannot be solved analytically and a numerical integration routine is employed. Equations (19) and (20) give the pressure at the surface of the cylindrical fuselage which is relevant for the assessment of cabin noise.

2. Total Far-Field

The same process is followed for the far-field case. Once again, the Fourier transformed total field is described by eq.(11). The Fourier transformed scattered field is given by eq.(14) as in the near-field case. However, for the far-field case the Fourier transformed incidence field in eq.(11) is given by eq.(9),

$$\begin{aligned}\overline{p'_{tn}}\left(\bar{r},k_z,t\right) &= \pi^2\xi_{lq}P_{lq}\,\mathrm{e}^{\mathrm{i}(n-l)\beta}\left(k_0+k_zM\right)\Psi_{lq}\,\mathrm{H}_n^{(2)}\left(\Gamma_0\bar{r}\right)\mathrm{e}^{\mathrm{i}\omega_0 t}\times \\ &\quad\left[\frac{\mathrm{J}_{n-l}\left(\Gamma_0 b\right)\mathrm{H}_n^{(2)\prime}\left(\Gamma_0 a_0\right)-\mathrm{H}_{n-l}^{(2)}\left(\Gamma_0 b\right)\mathrm{J}'_n\left(\Gamma_0 a_0\right)}{\mathrm{H}_n^{(2)\prime}\left(\Gamma_0 a_0\right)}\right].\end{aligned} \tag{21}$$

Again the total far-field pressure in real space is obtained by using eq.(15) substituting $\overline{p'_{tn}}\left(\bar{r},k_z,t\right)$ with its expression in eq.(21). The resulting inverse Fourier z-transform integral in eq.(15) can be solved asymptotically by employing spherical polar coordinates and a large argument approximation for the Hankel function term which is dependent on $\bar{r}$. This expresses the integral in an appropriate form to be solved by applying the method of stationary phase, as shown in the appendix. The final far-field expression in terms of spherical polar coordinates is

$$\begin{aligned}p'_t\left(\bar{R},\bar{\theta},\bar{\phi},t\right) &= \frac{\mathrm{i}\xi_{lq}P_{lq}k_0}{2\bar{R}}\,\Psi_{lq}(\Delta_0)\,\frac{S(\bar{\theta})}{\left(1-M^2\sin^2\bar{\theta}\right)}\sum_{n=-\infty}^{\infty}\mathrm{e}^{\mathrm{i}(n-l)\beta}\,\mathrm{e}^{\frac{1}{2}n\pi\mathrm{i}}\,\mathrm{e}^{\mathrm{i}\omega_0 t}\times \\ &\quad\mathrm{e}^{-\mathrm{i}k_0\bar{R}S(\bar{\theta})}\,\mathrm{e}^{-\mathrm{i}n\bar{\phi}}\left[\frac{\mathrm{J}_{n-l}\left(\Delta_0 b\right)\mathrm{H}_n^{(2)\prime}\left(\Delta_0 a_0\right)-\mathrm{H}_{n-l}^{(2)}\left(\Delta_0 b\right)\mathrm{J}'_n\left(\Delta_0 a_0\right)}{\mathrm{H}_n^{(2)\prime}\left(\Delta_0 a_0\right)}\right],\end{aligned} \tag{22}$$

where $\Delta_0 = \frac{k_0\sin\bar{\theta}}{\left(1-M^2\sin^2\bar{\theta}\right)^{1/2}}$ and $S(\bar{\theta}) = \frac{\left(\left(1-M^2\sin^2\bar{\theta}\right)^{1/2}+M\cos\bar{\theta}\right)}{\sigma^2}$. This far-field expression is expressed in terms of a Fourier series and has been validated by reducing the disc source to a point source. When this is performed, after considerable algebraic manipulaton, eq.(22) reduces to the known solution for a stationary monopole adjacent to a cylinder given by Bowman (page 127, eq.(2.149) from Ref. [18]).

C. Linear Boundary Layer Profile Analysis

According to previous research ([3], [4], [10], [11]) the refraction effect due to the presence of a boundary layer on the fuselage cannot be ignored. Experimental data on fuselage pressure presented in Ref. [4] show a substantial discrepancy between the theoretical results and the measurements upstream of the engine source. That is because the theoretical results were based on a uniform flow assumption and did not take into account the presence of the boundary layer on the fuselage. All previous work used numerical methods to solve the equation that governs propagation inside the boundary layer, namely the Pridmore-Brown equation [13]

$$\frac{\mathrm{D}_0}{\mathrm{D}t}\left(\frac{\mathrm{D}_0{}^2p}{\mathrm{D}t^2}-\nabla^2p\right)-2M'\frac{\partial^2p}{\partial\bar{r}\partial\bar{z}}=0, \tag{23}$$

where $M' = \mathrm{d}M/\mathrm{d}\bar{r}$ is the Mach number gradient. In this paper the key analysis is an analytical approach to solve the Pridmore-Brown equation. This is possible, but subject to constraints. Eversman and Beckemeyer [12] proposed an asymptotic method that was proven to be accurate for sufficiently thin boundary layers. The work presented here is based on this method and applied to a linear velocity profile. That will simplify the calculations and facilitate quicker results in contrary to previous numerical work. Also, by allowing a slip velocity at the wall, the linear profile can be used to simulate other profiles such as the quarter-sine or the 1/7th power law.

1. Power Series Solution

The analysis is applied to a linear boundary layer with slip on the wall M_w and free stream Mach number M_0. A sketch of the linear boundary layer problem is shown in Fig. (4). The Mach number profile inside the linear boundary layer is defined as

$$M = M_0\varphi(\zeta) = M_0\left(\zeta\frac{M_0-M_w}{M_0}+\frac{M_w}{M_0}\right). \tag{24}$$

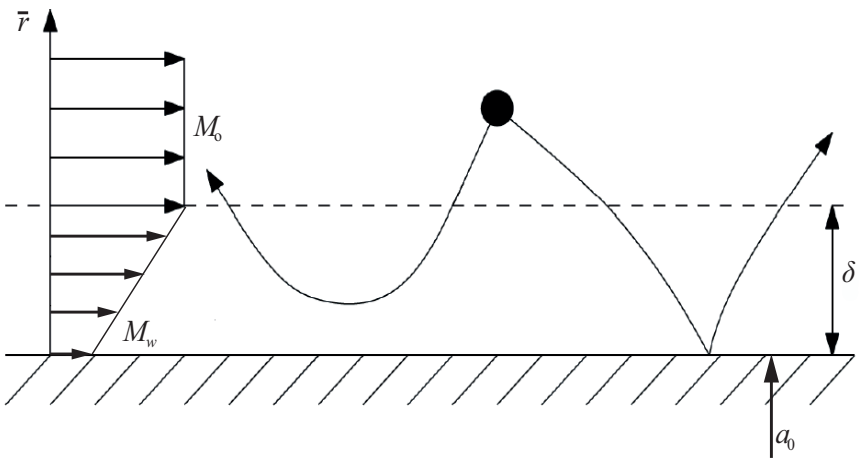

Fig. 4 Boundary layer with linear velocity profile.

The Fourier transformed Pridmore-Brown equation expressed in cylindrical polar coordinates describes the total field inside the boundary layer

$$\frac{\mathrm{d}^2\overline{p'_{t_{in}}}}{\mathrm{d}\bar{r}^2} + \left(\frac{1}{\bar{r}} - \frac{2k_z M'}{k_0 + k_z M}\right)\frac{\mathrm{d}\overline{p'_{t_{in}}}}{\mathrm{d}\bar{r}} + \left[(k_0 + k_z M)^2 - k_z^2 - \frac{n^2}{\bar{r}^2}\right]\overline{p'_{t_{in}}} = 0. \tag{25}$$

The initial part of the analysis is to change variables firstly to $y = \frac{\bar{r}-a_0}{a_0}$, and then to $\zeta = \frac{y}{\varepsilon}$, with the parameter

$$\varepsilon = \frac{\delta}{a_0}, \tag{26}$$

which is the non-dimenional boundary layer thickness. This change of variable is performed in order to shift the limits of the boundary layer from $a_0 < \bar{r} < a_0 + \delta$ to $0 < \zeta < 1$.

With these changes, eq.(25) becomes

$$\frac{\mathrm{d}^2\overline{p'_{t_{in}}}}{\mathrm{d}\zeta^2} + \left(\frac{\varepsilon}{\varepsilon\zeta + 1} - \frac{2KM_0}{1 + KM}\frac{\mathrm{d}\varphi}{\mathrm{d}\zeta}\right)\frac{\mathrm{d}\overline{p'_{t_{in}}}}{\mathrm{d}\zeta} + \varepsilon^2\left\{(k_0 a_0)^2\left[(1 + KM)^2 - K^2\right] - \frac{n^2}{(\varepsilon\zeta + 1)^2}\right\}\overline{p'_{t_{in}}} = 0, \tag{27}$$

where $K = k_z/k_0$. The boundary condition at the fuselage surface is a rigid hard-wall boundary condition, which means

$$\frac{\mathrm{d}\overline{p'_{t_{in}}}}{\mathrm{d}\zeta} = 0 \ \text{ at } \ \zeta = 0, \tag{28}$$

because $\bar{r} = a_0 \Rightarrow \zeta = 0$ by definition.

Following Eversman and Beckemeyer [12], eq.(27) can be solved using a power series solution in ε of the form,

$$\overline{p'_{t_{in}}}(\zeta) = \overline{p'_0}(\zeta) + \varepsilon\overline{p'_1}(\zeta) + \varepsilon^2\overline{p'_2}(\zeta) + \varepsilon^3\overline{p'_3}(\zeta) + \ldots, \tag{29}$$

with a slight abuse of notation, omitting for convenience the arguments k_z and t of $\overline{p'_{t_{in}}}$ and also the $\exp\{\mathrm{i}\omega_0 t\}$ dependence. By substituting this solution into eq.(27) and eq.(28) and equating the same powers of ε, differential equations and boundary conditions can be obtained for each of the terms in the power series.

Zeroth order:

$$\frac{\mathrm{d}^2\overline{p'_0}}{\mathrm{d}\zeta^2} - \frac{2KM_0}{1 + KM_0\varphi}\frac{\mathrm{d}\varphi}{\mathrm{d}\zeta}\frac{\mathrm{d}\overline{p'_0}}{\mathrm{d}\zeta} = 0, \tag{30}$$

$$\frac{\mathrm{d}\overline{p'_0}}{\mathrm{d}\zeta}(\zeta = 0) = 0. \tag{31}$$

First order:

$$\frac{\mathrm{d}^2\overline{p_1'}}{\mathrm{d}\zeta^2} - \frac{2KM_0}{1+KM_0\varphi}\frac{\mathrm{d}\varphi}{\mathrm{d}\zeta}\frac{\mathrm{d}\overline{p_1'}}{\mathrm{d}\zeta} = -\frac{\mathrm{d}\overline{p_0'}}{\mathrm{d}\zeta}, \tag{32}$$

$$\frac{\mathrm{d}\overline{p_1'}}{\mathrm{d}\zeta}(\zeta=0) = 0. \tag{33}$$

Second order:

$$\frac{\mathrm{d}^2\overline{p_2'}}{\mathrm{d}\zeta^2} - \frac{2KM_0}{1+KM_0\varphi}\frac{\mathrm{d}\varphi}{\mathrm{d}\zeta}\frac{\mathrm{d}\overline{p_2'}}{\mathrm{d}\zeta} = -\frac{\mathrm{d}\overline{p_1'}}{\mathrm{d}\zeta} + \zeta\frac{\mathrm{d}\overline{p_0'}}{\mathrm{d}\zeta} - X\overline{p_0'} + n^2\overline{p_0'}, \quad X = (k_0a_0)^2\Big[(1+KM_0\varphi)^2 - K^2\Big], \tag{34}$$

$$\frac{\mathrm{d}\overline{p_2'}}{\mathrm{d}\zeta}(\zeta=0) = 0. \tag{35}$$

Third order:

$$\frac{\mathrm{d}^2\overline{p_3'}}{\mathrm{d}\zeta^2} - \frac{2KM_0}{1+KM_0\varphi}\frac{\mathrm{d}\varphi}{\mathrm{d}\zeta}\frac{\mathrm{d}\overline{p_3'}}{\mathrm{d}\zeta} = -\frac{\mathrm{d}\overline{p_2'}}{\mathrm{d}\zeta} + \zeta\frac{\mathrm{d}\overline{p_1'}}{\mathrm{d}\zeta} - \zeta^2\frac{\mathrm{d}\overline{p_0'}}{\mathrm{d}\zeta} - X\overline{p_1'} + n^2\overline{p_1'} - 2\zeta n^2\overline{p_0'}, \tag{36}$$

$$\frac{\mathrm{d}\overline{p_3'}}{\mathrm{d}\zeta}(\zeta=0) = 0. \tag{37}$$

By arbitrarily specifying the pressure at the wall, for the zeroth-order term

$$\overline{p_0'}(\zeta=0) = \overline{p_{t_{in}}'}(0), \tag{38}$$

and for the higher-order terms

$$\begin{aligned} &\overline{p_1'}(\zeta=0) = 0, \\ &\overline{p_2'}(\zeta=0) = 0 \quad \text{etc.} \end{aligned} \tag{39}$$

Each term in the power series can be determined by systematically solving the set of differential equations and boundary conditions (eqs.(30–37).

Zeroth order:

$$\begin{aligned} \frac{\mathrm{d}\overline{p_0'}}{\mathrm{d}\zeta} = 0 \qquad &\Rightarrow \qquad \overline{p_0'}(\zeta) = \text{constant}, \\ &\Rightarrow \qquad \overline{p_0'}(\zeta) = \overline{p_{t_{in}}'}(0). \end{aligned} \tag{40}$$

First order:

$$\begin{aligned} \frac{\mathrm{d}\overline{p_1'}}{\mathrm{d}\zeta} = 0 \qquad &\Rightarrow \qquad \overline{p_1'}(\zeta) = \text{constant}, \\ &\Rightarrow \qquad \overline{p_1'}(\zeta) = 0. \end{aligned} \tag{41}$$

Second order:

$$\frac{\mathrm{d}\overline{p_2'}}{\mathrm{d}\zeta} = \overline{p_{t_{in}}'}(0)(1+KM_0\varphi)^2\Big[\mu\int_0^\zeta \frac{\mathrm{d}\eta}{(1+KM_0\varphi(\eta))^2} - \nu\zeta\Big], \tag{42}$$

$$\Rightarrow \quad \overline{p_2'}(\zeta) = \overline{p_{t_{in}}'}(0)\int_0^\zeta \left\{(1+KM_0\varphi(\sigma))^2\Big[\mu\int_0^\sigma \frac{\mathrm{d}\eta}{(1+KM_0\varphi(\eta))^2} - \nu\sigma\Big]\right\}\mathrm{d}\sigma. \tag{43}$$

Third order:

$$\frac{\mathrm{d}\overline{p_3'}}{\mathrm{d}\zeta} = -\overline{p'_{t_{in}}}(0)(1+KM_0\varphi)^2\Big\{\int_0^\zeta\Big[\mu\int_0^\xi\frac{\mathrm{d}\eta}{(1+KM_0\varphi(\eta))^2}-\nu\xi\Big]\mathrm{d}\xi+2\int_0^\zeta\frac{mn^2}{(1+KM_0\varphi(m))^2}\mathrm{d}m\Big\}, \quad (44)$$

$$\Rightarrow \quad \overline{p_3'}(\zeta) = -\overline{p'_{t_{in}}}(0)\int_0^\zeta(1+KM_0\varphi(\sigma))^2\Big\{\int_0^\sigma\Big[\mu\int_0^\xi\frac{\mathrm{d}\eta}{(1+KM_0\varphi(\eta))^2}-\nu\xi\Big]\mathrm{d}\xi+ 2\int_0^\sigma\frac{mn^2}{(1+KM_0\varphi(m))^2}\mathrm{d}m\Big\}\mathrm{d}\sigma. \quad (45)$$

Note that in eqs. (42–45)

$$\nu = (k_0a_0)^2 \quad \text{and} \quad \mu = (k_0a_0)^2K^2+n^2. \quad (46)$$

With these terms known, the power series expression can be evaluated. For the pressure, up to the second order terms are retained in order to have an error of $O(\varepsilon^3)$,

$$\overline{p'_{t_{in}}}(\zeta) = \overline{p'_0}(\zeta)+\varepsilon\overline{p'_1}(\zeta)+\varepsilon^2\overline{p'_2}(\zeta). \quad (47)$$

Substituting eqs. (40), (41) and (43) into eq. (47) gives

$$\overline{p'_{t_{in}}}(\zeta) = \overline{p'_{t_{in}}}(0)\left\{1+\varepsilon^2\int_0^\zeta\left[(1+KM_0\varphi(\sigma))^2\Big[\mu\int_0^\sigma\frac{\mathrm{d}\eta}{(1+KM_0\varphi(\eta))^2}-\nu\sigma\Big]\right]\mathrm{d}\sigma\right\}. \quad (48)$$

In order to retain comparative relative error, following Eversman and Beckemeyer [12], the expression for the pressure derivative is carried to within an error of $O(\varepsilon^4)$,

$$\frac{\mathrm{d}\overline{p'_{t_{in}}}}{\mathrm{d}\zeta}(\zeta) = \frac{\mathrm{d}\overline{p'_0}}{\mathrm{d}\zeta}(\zeta)+\varepsilon\frac{\mathrm{d}\overline{p'_1}}{\mathrm{d}\zeta}(\zeta)+\varepsilon^2\frac{\mathrm{d}\overline{p'_2}}{\mathrm{d}\zeta}(\zeta)+\varepsilon^3\frac{\mathrm{d}\overline{p'_3}}{\mathrm{d}\zeta}(\zeta). \quad (49)$$

Substituting the terms from eqs. (40), (41), (42) and (44) into eq. (49) gives,

$$\begin{aligned}\frac{\mathrm{d}\overline{p'_{t_{in}}}}{\mathrm{d}\zeta}(\zeta) =&\varepsilon^2\overline{p'_{t_{in}}}(0)(1+KM_0\varphi)^2\left\{\left[\mu\int_0^\zeta\frac{\mathrm{d}\eta}{(1+KM_0\varphi(\eta))^2}-\nu\zeta\right]\right.\\ &\left.-\varepsilon\left[\int_0^\zeta\Big[\mu\int_0^\xi\frac{\mathrm{d}\eta}{(1+KM_0\varphi(\eta))^2}-\nu\xi\Big]\mathrm{d}\xi+2n^2\int_0^\zeta\frac{m}{(1+KM_0\varphi(m))^2}\mathrm{d}m\right]\right\}.\end{aligned} \quad (50)$$

The integrals in eqs. (48) and (50) need to be evaluated in order to obtain expressions for the pressure and its derivative as a function of ζ.

Before the integrals are evaluated, the following quantities are introduced to facilitate the integrations. These quantities are

$$s = K(M_0-M_w), \quad (51)$$

and

$$g = K(M_0-M_w)(1+KM_w) = s(1+KM_w). \quad (52)$$

This will transform the term $(1+KM_0\varphi)^2$ into

$$(1+KM_0\varphi)^2 = (1+K\zeta(M_0-M_w)+KM_w)^2 = (g/s+\zeta s)^2. \quad (53)$$

Then solving the integrals for the linear velocity profile leads to the power series Fourier transformed pressure as a function of ζ to within an error of $O(\varepsilon^3)$,

$$\overline{p'_{t_{in}}}(\zeta) = \overline{p'_{t_{in}}}(0)\left\{1+\varepsilon^2\left[-\nu s^2\frac{\zeta^4}{4}+\frac{\zeta^3}{3}\Big(\frac{s^2\mu}{g}-2\nu g\Big)+\frac{\zeta^2}{2}\Big(\mu-\nu\frac{g^2}{s^2}\Big)\right]\right\}. \quad (54)$$

Additionally the power series Fourier transformed pressure derivative as a function of ζ to within an error of $O(\varepsilon^4)$ is,

$$\begin{aligned}\frac{\mathrm{d}\overline{p'_{t_{in}}}}{\mathrm{d}\zeta}(\zeta) =& \varepsilon^2\overline{p'_{t_{in}}}(0)\left\{-\nu s^2\zeta^3+\zeta^2(\mu\frac{s^2}{g}-2\nu g)+\zeta(\mu-\nu g^2/s^2)\right.\\ &\left.-\varepsilon\left[(2n^2-\mu)\Big[(\zeta+g/s^2)^2\ln\Big(\frac{s^2\zeta}{g}+1\Big)-\zeta\frac{g}{s^2}\Big]-\nu s^2\frac{\zeta^4}{2}+\zeta^3(\mu\frac{s^2}{g}-\nu g)-\zeta^2\Big[2(n^2-\mu)+\frac{\nu}{2}\frac{g^2}{s^2}\Big]\right]\right\}.\end{aligned} \quad (55)$$

2. Matching of the Two Solutions

In order to match the two solutions at the edge of the boundary layer, $\bar{r} = a_0 + \delta$ or equivalently $\zeta = 1$, the pressure and its derivative at that point must be known. Therefore, $\overline{p'_{t_{in}}}$ and $\frac{\mathrm{d}\overline{p'_{t_{in}}}}{\mathrm{d}\bar{r}}$ in eqs. (54) and (55) are evaluated at $\zeta = 1$.

$$\overline{p'_{t_{in}}}(\zeta = 1) = \overline{p'_{t_{in}}}(0)\left\{1 + \varepsilon^2\left[\mu\left(\frac{s^2}{3g} + \frac{1}{2}\right) - \nu\left(\frac{s^2}{4} + \frac{2}{3}g + \frac{1}{2}\frac{g^2}{s^2}\right)\right]\right\}. \tag{56}$$

$$\begin{aligned}\frac{\mathrm{d}\overline{p'_{t_{in}}}}{\mathrm{d}\bar{r}}(\zeta = 1) =& \frac{\varepsilon}{a_0}\overline{p'_{t_{in}}}(0)(1 + KM_0)^2\left\{\mu\left(\frac{1}{g} - \frac{1}{(s^2 + g)}\right) - \nu\right. \\ & \left. - \varepsilon\left[\frac{(2n^2 - \mu)}{s^2}\ln\left(\frac{s^2 + g}{g}\right) - \frac{2n^2}{s^2 + g} + \frac{\mu}{g} - \frac{\nu}{2}\right]\right\}.\end{aligned} \tag{57}$$

Outside the boundary layer the mean flow is uniform and thus the total field can be expressed in terms of an incident and scattered field derived previously in Sec. B. The Fourier transformed incident field is given in eq.(6) or written alternatively as

$$\overline{p'_{i_{out}}}(\bar{r}) \;=\; E_n(k_z, \omega_0)\mathrm{J}_n(\Gamma_0\bar{r}), \tag{58}$$

again omitting the arguments k_z and t and the $\exp\{\mathrm{i}\omega_0 t\}$ dependence. where

$$E_n(k_z, \omega_0) = \pi^2\xi_{lq}P_{lq}(-1)^{l+n}(k_0 + k_z M_0)\,\Psi_{lq}\,\mathrm{e}^{-\mathrm{i}(l-n)\beta}\,\mathrm{H}^{(2)}_{l-n}(\Gamma_0 b). \tag{59}$$

On the other hand, the Fourier transformed scattered field is given in eq.(10), or written alternatively as

$$\overline{p'_{s_{out}}}(\bar{r}) \;=\; \frac{1}{2\pi}C_n(k_z, \omega_0)\mathrm{H}^{(2)}_n(\Gamma_0\bar{r}), \tag{60}$$

also with a different symbol used for the coefficient. (The coefficient is renamed because with the inclusion of the boundary layer, the coefficient is not the same as its value with uniform mean flow everywhere.)

Inside the boundary layer, the Fourier transformed total field is described in eqs. (54) and (55). The matching of the two solutions is essential in order to determine the two unknowns of the problem, namely the Fourier transformed pressure at the fuselage wall $\overline{p'_{t_{in}}}(0)$ in eqs. (54) and (55), and the coefficient $C_n(k_z, \omega_0)$ in eq.(60). The evaluation of $\overline{p'_{t_{in}}}(0)$ is one of the key results of the analysis in this paper since it specifies the pressure at the wall which is practically the most important part of the near-field solution.

The matching is performed by using two continuity conditions at the edge of the boundary layer, $\bar{r} = a_0 + \delta$ or equivalently $\zeta = 1$. The pressure continuity condition,

$$\overline{p'_{t_{in}}}(\zeta = 1) = \overline{p'_{t_{out}}}(\bar{r} = a_0 + \delta), \tag{61}$$

and the particle displacement continuity condition, which in the linear profile case reduces to a pressure gradient continuity condition,

$$\frac{\mathrm{d}\overline{p'_{t_{in}}}}{\mathrm{d}\bar{r}}(\zeta = 1) = \frac{\mathrm{d}\overline{p'_{t_{out}}}}{\mathrm{d}\bar{r}}(\bar{r} = a_0 + \delta). \tag{62}$$

Since the total Fourier transformed field outside the layer is the sum of the incident and the scattered field, the pressure continuity condition is expressed as

$$\overline{p'_{t_{in}}}(\zeta = 1) = \overline{p'_{i_{out}}}(\bar{r} = a_0 + \delta) + \overline{p'_{s_{out}}}(\bar{r} = a_0 + \delta), \tag{63}$$

and by substituting eqs. (56), (58) and (60) into eq.(63),

$$\begin{aligned}&\overline{p'_{t_{in}}}(0)\left\{1 + \varepsilon^2\left[\mu\left(\frac{s^2}{3g} + \frac{1}{2}\right) - \nu\left(\frac{s^2}{4} + \frac{2}{3}g + \frac{1}{2}\frac{g^2}{s^2}\right)\right]\right\} \\ &= E_n(k_z, \omega_0)\mathrm{J}_n(\Gamma_0(a_0 + \delta)) + \frac{1}{2\pi}C_n(k_z, \omega_0)\mathrm{H}^{(2)}_n(\Gamma_0(a_0 + \delta)).\end{aligned} \tag{64}$$

The same procedure is followed for the pressure gradient continuity condition,

$$\frac{\mathrm{d}\overline{p'_{t_{in}}}}{\mathrm{d}\bar{r}}(\zeta = 1) = \frac{\mathrm{d}\overline{p'_{i_{out}}}}{\mathrm{d}\bar{r}}(\bar{r} = a_0 + \delta) + \frac{\mathrm{d}\overline{p'_{s_{out}}}}{\mathrm{d}\bar{r}}(\bar{r} = a_0 + \delta), \tag{65}$$

and substituting eq.(57), (58) and (60) into eq.(65),

$$\begin{aligned}&\frac{\varepsilon}{a_0}\overline{p'_{t_{in}}}(0)(1+KM_0)^2\left\{\mu\left(\frac{1}{g}-\frac{1}{(s^2+g)}\right)-\nu-\varepsilon\left[\frac{(2n^2-\mu)}{s^2}\ln\left(\frac{s^2+g}{g}\right)-\frac{2n^2}{s^2+g}+\frac{\mu}{g}-\frac{\nu}{2}\right]\right\}\\&= E_n(k_z,\omega_0)\Gamma_0\mathrm{J}'_n\left(\Gamma_0(a_0+\delta)\right)+\frac{1}{2\pi}C_n(k_z,\omega_0)\Gamma_0\mathrm{H}_n^{(2)\prime}\left(\Gamma_0(a_0+\delta)\right),\end{aligned} \tag{66}$$

Using eqs. (64) and (66), solving for $\overline{p'_{t_{in}}}(0)$ and $C_n(k_z,\omega_0)$ leads to

$$\begin{aligned}\overline{p'_{t_{in}}}(0) = \frac{E_n(k_z,\omega_0)}{G}\Bigg[&\mathrm{J}_n\left(\Gamma_0(a_0+\delta)\right)\\&+\frac{\left[\mathrm{J}'_n\left(\Gamma_0(a_0+\delta)\right)-\frac{R}{G}\frac{\varepsilon}{\Gamma_0 a_0}(1+KM_0)^2\mathrm{J}_n\left(\Gamma_0(a_0+\delta)\right)\right]}{\left[\frac{R}{G}\frac{\varepsilon}{\Gamma_0 a_0}(1+KM_0)^2\mathrm{H}_n^{(2)}\left(\Gamma_0(a_0+\delta)\right)-\mathrm{H}_n^{(2)\prime}\left(\Gamma_0(a_0+\delta)\right)\right]}\mathrm{H}_n^{(2)}\left(\Gamma_0(a_0+\delta)\right)\Bigg],\end{aligned} \tag{67}$$

where

$$G = \left\{1+\varepsilon^2\left[\mu\left(\frac{s^2}{3g}+\frac{1}{2}\right)-\nu\left(\frac{s^2}{4}+\frac{2}{3}g+\frac{1}{2}\frac{g^2}{s^2}\right)\right]\right\}, \tag{68}$$

and

$$R = \left\{\mu\left(\frac{1}{g}-\frac{1}{(s^2+g)}\right)-\nu-\varepsilon\left[\frac{(2n^2-\mu)}{s^2}\ln\left(\frac{s^2+g}{g}\right)-\frac{2n^2}{s^2+g}+\frac{\mu}{g}-\frac{\nu}{2}\right]\right\}. \tag{69}$$

The evaluation of $\overline{p'_{t_{in}}}(0)$ is a key result of this part of the work. However, it is important to mention the other quantities that can be determined. The Fourier transformed scattered field is essential for the evaluation of the far-field case. The coefficient $C_n(k_z,\omega_0)$ is

$$C_n(k_z,\omega_0) = \frac{2\pi E_n(k_z,\omega_0)\left[\mathrm{J}'_n\left(\Gamma_0(a_0+\delta)\right)-\frac{R}{G}\frac{\varepsilon}{\Gamma_0 a_0}(1+KM_0)^2\mathrm{J}_n\left(\Gamma_0(a_0+\delta)\right)\right]}{\left[\frac{R}{G}\frac{\varepsilon}{\Gamma_0 a_0}(1+KM_0)^2\mathrm{H}_n^{(2)}\left(\Gamma_0(a_0+\delta)\right)-\mathrm{H}_n^{(2)\prime}\left(\Gamma_0(a_0+\delta)\right)\right]}. \tag{70}$$

Thus, the Fourier transformed scattered field is given from eq.(60) upon substituting $C_n(k_z,\omega_0)$ with its expression from eq.(70),

$$\overline{p'_{s_{out}}}(\bar{r}) = \frac{E_n(k_z,\omega_0)\left[\mathrm{J}'_n\left(\Gamma_0(a_0+\delta)\right)-\frac{R}{G}\frac{\varepsilon}{\Gamma_0 a_0}(1+KM_0)^2\mathrm{J}_n\left(\Gamma_0(a_0+\delta)\right)\right]}{\left[\frac{R}{G}\frac{\varepsilon}{\Gamma_0 a_0}(1+KM_0)^2\mathrm{H}_n^{(2)}\left(\Gamma_0(a_0+\delta)\right)-\mathrm{H}_n^{(2)\prime}\left(\Gamma_0(a_0+\delta)\right)\right]}\mathrm{H}_n^{(2)}\left(\Gamma_0\bar{r}\right). \tag{71}$$

Before moving on, an initial validation can be performed at this point by taking the limit as $\delta \to 0$ in eqs. (67) and (71). When the boundary layer vanishes then the expressions should reduce to the uniform flow expressions given by McAlpine et al. [8] and outlined in Sec. B. Therefore, it is expected that when $\delta \to 0$, eq.(67) reduces to eq.(18). Also, eq.(71) will reduce to eq.(14) which is the scattered field for uniform flow.

Firstly, the bracketed terms G and R are evaluated in the limit as $\delta \to 0$. Considering that $\delta \to 0$ also means that $\varepsilon \to 0$, by definition

$$\lim_{\varepsilon\to 0} G = 1, \tag{72}$$

and

$$\lim_{\varepsilon\to 0} R = \left\{\mu\left(\frac{1}{g}-\frac{1}{(s^2+g)}\right)-\nu\right\}. \tag{73}$$

Therefore, when $\delta \to 0$ or $\varepsilon \to 0$, eq.(67) becomes

$$\overline{p'_{t_{in}}}(0) = E_n(k_z, \omega_0)\left[\mathrm{J}_n\left(\Gamma_0 a_0\right) + \frac{\mathrm{J}'_n\left(\Gamma_0 a_0\right)}{-\mathrm{H}_n^{(2)\prime}\left(\Gamma_0 a_0\right)}\mathrm{H}_n^{(2)}\left(\Gamma_0 a_0\right)\right], \tag{74}$$

and using the Wronskian formula, it reduces to

$$\overline{p'_{t_{in}}}(\bar{r} = a_0, k_z) = E_n(k_z, \omega_0)\left[\frac{-\mathrm{i}2}{\pi\Gamma_0 a_0 \mathrm{H}_n^{(2)\prime}\left(\Gamma_0 a_0\right)}\right], \tag{75}$$

which is the same as eq.(18). On the other hand, by taking eq.(71) when $\delta \to 0$ or $\varepsilon \to 0$,

$$\overline{p'_{s_{out}}}\left(\bar{r}, k_z\right) = -E_n(k_z, \omega_0)\frac{\mathrm{J}'_n\left(\Gamma_0 a_0\right)}{\mathrm{H}_n^{(2)\prime}\left(\Gamma_0 a_0\right)}\mathrm{H}_n^{(2)}\left(\Gamma_0 \bar{r}\right), \tag{76}$$

which is the same as eq.(14).

3. Fuselage Surface Pressure

Equation (67) represents the Fourier transformed pressure on the fuselage surface. In order to obtain the pressure in real space an inverse Fourier z-transform must be performed. The dependence on $\bar{\phi}$ is represented as always, in the form of a Fourier series. Thus, following from eq.(15), the pressure on the fuselage surface is

$$p'_{t_{in}}\left(a_0, \bar{\phi}, \bar{z}, t\right) \;=\; \frac{1}{(2\pi)^2}\sum_{n=-\infty}^{\infty}\int_{-\infty}^{\infty}\overline{p'_{t_{in}}}\left(a_0, k_z\right)\mathrm{e}^{-\mathrm{i}k_z\bar{z}}\,\mathrm{d}k_z\,\mathrm{e}^{-\mathrm{i}n\bar{\phi}}\,\mathrm{e}^{\mathrm{i}\omega_0 t}, \tag{77}$$

which becomes, using eq.(67),

$$\begin{aligned} p'_{t_{in}}\left(a_0, \bar{\phi}, \bar{z}, t\right) =& \frac{1}{(2\pi)^2}\sum_{n=-\infty}^{\infty}\int_{-\infty}^{\infty}E_n(k_z, \omega_0)\Bigg[\mathrm{J}_n\left(\Gamma_0(a_0+\delta)\right)\frac{1}{G} \\ &+ \frac{\left[\mathrm{J}'_n\left(\Gamma_0(a_0+\delta)\right) - \frac{R}{G}\frac{\varepsilon}{\Gamma_0 a_0}(1+KM_0)^2\mathrm{J}_n\left(\Gamma_0(a_0+\delta)\right)\right]}{\left[\frac{R}{G}\frac{\varepsilon}{\Gamma_0 a_0}(1+KM_0)^2\mathrm{H}_n^{(2)}\left(\Gamma_0(a_0+\delta)\right) - \mathrm{H}_n^{(2)\prime}\left(\Gamma_0(a_0+\delta)\right)\right]}\frac{\mathrm{H}_n^{(2)}\left(\Gamma_0(a_0+\delta)\right)}{G}\Bigg] \\ &\times \mathrm{e}^{-\mathrm{i}k_z\bar{z}}\,\mathrm{d}k_z\,\mathrm{e}^{-\mathrm{i}n\bar{\phi}}\,\mathrm{e}^{\mathrm{i}\omega_0 t}. \end{aligned} \tag{78}$$

This can be written in compact form as

$$p'_{t_{in}}\left(a_0, \bar{\phi}, \bar{z}, t\right) = \frac{\xi_{lq}P_{lq}}{4}(-1)^l\mathrm{e}^{-\mathrm{i}l\beta}\sum_{n=-\infty}^{\infty}(-1)^n\mathrm{e}^{\mathrm{i}n\beta}I_n^{(lbl)}(a_0, \bar{z})\mathrm{e}^{-\mathrm{i}n\bar{\phi}}\,\mathrm{e}^{\mathrm{i}\omega_0 t}, \tag{79}$$

where

$$I_n^{(lbl)}(a_0, \bar{z}) = \int_{-\infty}^{\infty}(k_0 + k_z M_0)\,\Psi_{lq}\;\mathrm{H}_{l-n}^{(2)}\left(\Gamma_0 b\right)S_n(k_z, \omega_0)\mathrm{e}^{-\mathrm{i}k_z\bar{z}}\,\mathrm{d}k_z, \tag{80}$$

and

$$\begin{aligned} S_n(k_z, \omega_0) =& \Bigg[\mathrm{J}_n\left(\Gamma_0(a_0+\delta)\right)\frac{1}{G} \\ &+ \frac{\left[\mathrm{J}'_n\left(\Gamma_0(a_0+\delta)\right) - \frac{R}{G}\frac{\varepsilon}{\Gamma_0 a_0}(1+KM_0)^2\mathrm{J}_n\left(\Gamma_0(a_0+\delta)\right)\right]}{\left[\frac{R}{G}\frac{\varepsilon}{\Gamma_0 a_0}(1+KM_0)^2\mathrm{H}_n^{(2)}\left(\Gamma_0(a_0+\delta)\right) - \mathrm{H}_n^{(2)\prime}\left(\Gamma_0(a_0+\delta)\right)\right]}\frac{\mathrm{H}_n^{(2)}\left(\Gamma_0(a_0+\delta)\right)}{G}\Bigg]. \end{aligned} \tag{81}$$

The inverse Fourier z-transform integral in eq. (80) with the superscript (lbl) denoting *linear boundary layer* cannot be solved analytically, which means that a numerical integration routine is required to evaluate it. It is important to note that the integrand contains certain singularity points along the k_z-axis, but all the singularities are integrable.

Finally, it is important to note that the expressions derived here contain the logarithm term $\ln\left(\frac{s^2+g}{g}\right)$. This poses a potential issue, because the argument of the logarithm can become negative, in which case the logarithm would become imaginary.

The region where this happens coincides with the region where there is the critical layer. For the linear boundary layer the critical layer lies in the region $-k_0/M_W < k_z < -k_0/M_0$ as shown in Fig. (5). The critical layer is the point at which $k_0 + k_z M(\bar{r}_c) = 0$. At this point the Pridmore-Brown equation is no longer valid and thus cannot be used to describe the pressure field. Previous researchers ([4], [6], [7], [10], [11]) utilised a power series solution around the singularity in order to bridge it, namely a Frobenius solution.

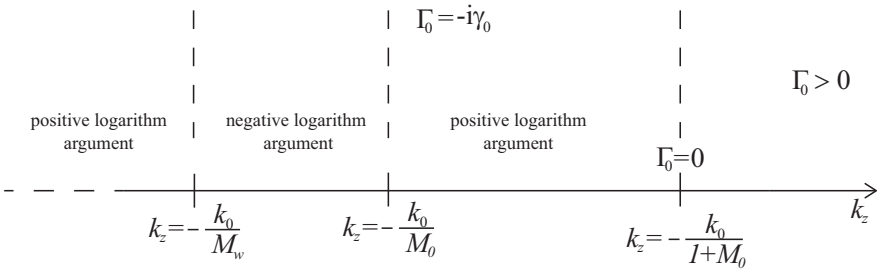

Fig. 5 Critical layer along the k_z-axis.

However, according to Gaffney [14] the critical layer region contributes very little to the integrand in eq.(80). That led to the conclusion that the inclusion of the critical layer region in the integration can be onitted without significant loss in the accuracy. Although the solution with the critical layer is currently under investigation, the work presented here does not include it. In order to ensure that, the lower limit of the integral in eq.(80) is truncated before the critical layer region.

4. Total Far-Field

The same procedure is followed for the far-field, except the incident field has a different form, given in eq.(9). This is written alternatively as

$$\overline{p'_{i_{nff}}}\,(\bar{r}, k_z) \;=\; \pi^2 \xi_{lq} P_{lq}\,(k_0 + k_z M_0)\,\Psi_{lq}\,\mathrm{e}^{\mathrm{i}(n-l)\beta}\,\mathrm{J}_{n-l}\,(\Gamma_0 b)\,\mathrm{H}_n^{(2)}\,(\Gamma_0 \bar{r}) \quad \text{for} \quad \bar{r} > b. \tag{82}$$

The scattered field is unchanged because there are no restrictions on the radiation condition. The Fourier transformed scattered field outside the boundary layer (which is the scattered field that radiates to the far-field) is given in eq.(71) with the subscript ff added for clarity to denote far field.

Thus, the total Fourier transformed far-field pressure is

$$\overline{p'_{t_{nff}}}\,(\bar{r}, k_z) = \overline{p'_{i_{nff}}}\,(\bar{r}, k_z) + \overline{p'_{s_{nff}}}\,(\bar{r}, k_z), \tag{83}$$

which leads to

$$\begin{aligned}\overline{p'_{t_{nff}}}\,(\bar{r}, k_z) = F_n(k_z, \omega_0)\Bigg[&\mathrm{J}_{n-l}\,(\Gamma_0 b) \\ &+ \mathrm{H}_{n-l}^{(2)}\,(\Gamma_0 b)\frac{\left[\mathrm{J}'_n\,(\Gamma_0(a_0+\delta)) - \frac{R}{G}\frac{\varepsilon}{\Gamma_0 a_0}(1+KM_0)^2\mathrm{J}_n\,(\Gamma_0(a_0+\delta))\right]}{\left[\frac{R}{G}\frac{\varepsilon}{\Gamma_0 a_0}(1+KM_0)^2\mathrm{H}_n^{(2)}\,(\Gamma_0(a_0+\delta)) - \mathrm{H}_n^{(2)\prime}\,(\Gamma_0(a_0+\delta))\right]}\Bigg]\mathrm{H}_n^{(2)}\,(\Gamma_0 \bar{r}),\end{aligned} \tag{84}$$

where

$$F_n(k_z, \omega_0) = \pi^2 \xi_{lq} P_{lq}\,(k_0 + k_z M_0)\,\Psi_{lq}\,\mathrm{e}^{-\mathrm{i}(l-n)\beta}. \tag{85}$$

Following the same procedure as in the near-field case, an inverse Fourier z-transform must be performed in order to obtain the total field in real space, i.e.

$$p'_{t_{ff}}\,(\bar{r}, \bar{\phi}, \bar{z}, t) \;=\; \frac{1}{(2\pi)^2}\sum_{n=-\infty}^{\infty}\int_{-\infty}^{\infty}\overline{p'_{t_{nff}}}\,(\bar{r}, k_z)\,\mathrm{e}^{-\mathrm{i}k_z\bar{z}}\,\mathrm{d}k_z\,\mathrm{e}^{-\mathrm{i}n\bar{\phi}}\,\mathrm{e}^{\mathrm{i}\omega_0 t}. \tag{86}$$

As in the uniform flow case, the integral

$$I_n \;=\; \frac{1}{2\pi}\int_{-\infty}^{\infty}\overline{p'_{t_{nff}}}\,(\bar{r},k_z)\,\mathrm{e}^{-\mathrm{i}k_z\bar{z}}\,\mathrm{d}k_z. \tag{87}$$

is in the appropriate form to be evaluated by the method of stationery phase as presented in section VI.D of the appendix. In fact the procedure is exactly the same, the only difference being the bracketed term in eq.(139) of section VI.D in the appendix is relaced with the bracketed term in eq.(84). Also, the similarity variables are the same with M replaced by M_0. The rest of the procedure is unchanged and presented in the appendix.

Thus the final total far-field in real space is

$$p'_{t_{ff}}\,(\bar{R},\bar{\theta},\bar{\phi},t) = \frac{\mathrm{i}\xi_{lq}P_{lq}k_0}{2\bar{R}}\frac{S(\bar{\theta})}{\Theta}\Psi_{lq}(\Delta_0)\mathrm{e}^{-\mathrm{i}k_0\bar{R}S(\bar{\theta})}\mathrm{e}^{\mathrm{i}\omega_0 t}\sum_{n=-\infty}^{\infty}\mathfrak{C}_n(\bar{\theta})\mathrm{e}^{-\mathrm{i}(l-n)\beta}\mathrm{e}^{\frac{1}{2}n\pi\mathrm{i}}\mathrm{e}^{-\mathrm{i}n\bar{\phi}}, \tag{88}$$

where

$$\mathfrak{C}_n(\bar{\theta}) = \left[\mathrm{J}_{n-l}\,(\Delta_0 b) + \mathrm{H}^{(2)}_{n-l}\,(\Delta_0 b)\frac{\left[\mathrm{J}'_n\,(\Delta_0(a_0+\delta)) - \frac{R(\bar{\theta})}{G(\bar{\theta})}\frac{\varepsilon(\Theta^{1/2}+M_0C(\bar{\theta}))^2}{k_0 a_0\sin\bar{\theta}\Theta^{1/2}}\mathrm{J}_n\,(\Delta_0(a_0+\delta))\right]}{\left[\frac{R(\bar{\theta})}{G(\bar{\theta})}\frac{\varepsilon(\Theta^{1/2}+M_0C(\bar{\theta}))^2}{k_0 a_0\sin\bar{\theta}\Theta^{1/2}}\mathrm{H}^{(2)}_n\,(\Delta_0(a_0+\delta)) - \mathrm{H}^{(2)\prime}_n\,(\Delta_0(a_0+\delta))\right]}\right], \tag{89}$$

with

$$\begin{aligned} G(\bar{\theta}) =& \left\{1+\varepsilon^2\left[\left(n^2+\nu\frac{C^2(\bar{\theta})}{\Theta}\right)\left[\frac{C(\bar{\theta})(2M_0+M_w)+3\Theta^{1/2}}{6\left(\Theta^{1/2}+M_wC(\bar{\theta})\right)}\right]\right.\right. \\ &\left.\left. -\frac{\nu}{\Theta}\left[\frac{C^2(\bar{\theta})(M_0-M_w)^2}{4}+\left(\Theta^{1/2}+M_wC(\bar{\theta})\right)\left(C(\bar{\theta})(\frac{2}{3}M_0-\frac{1}{6}M_w)+\frac{1}{2}\Theta^{1/2}\right)\right]\right]\right\}, \end{aligned} \tag{90}$$

and

$$\begin{aligned} R(\bar{\theta}) =& \left\{\frac{\nu C^2(\bar{\theta})+n^2\Theta}{\left(\Theta^{1/2}+M_wC(\bar{\theta})\right)\left(\Theta^{1/2}+M_0C(\bar{\theta})\right)}-\nu\right. \\ &-\varepsilon\left[\frac{n^2\Theta}{C^2(\bar{\theta})(M_0-M_w)}\left[C(\bar{\theta})\left(\frac{C(\bar{\theta})(M_0-2M_w)-\Theta^{1/2}}{\left(\Theta^{1/2}+M_wC(\bar{\theta})\right)\left(\Theta^{1/2}+M_0C(\bar{\theta})\right)}\right)+\frac{1}{(M_0-M_w)}\ln\left(\frac{\Theta^{1/2}+M_0C(\bar{\theta})}{\Theta^{1/2}+M_wC(\bar{\theta})}\right)\right]\right. \\ &\left.\left.+\frac{\nu}{(M_0-M_w)}\left[\frac{C(\bar{\theta})}{\left(\Theta^{1/2}+M_wC(\bar{\theta})\right)}-\frac{(M_0-M_w)}{2}-\frac{1}{(M_0-M_w)}\ln\left(\frac{\Theta^{1/2}+M_0C(\bar{\theta})}{\Theta^{1/2}+M_wC(\bar{\theta})}\right)\right]\right]\right\}. \end{aligned} \tag{91}$$

Also, $\Delta_0 \;=\; \frac{k_0\sin\bar{\theta}}{(1-M^2\sin^2\bar{\theta})^{1/2}}$, $\Theta=(1-M_0^2\sin^2\bar{\theta})$, $S(\bar{\theta})=\frac{\left(\Theta^{1/2}+M_0\cos\bar{\theta}\right)}{\sigma_0^2}$, $C(\bar{\theta})=\frac{\left(\cos\bar{\theta}+M_0\Theta^{1/2}\right)}{\sigma_0^2}$ and $\sigma_0^2=1-M_0^2$.

Note that eq.(88) is the same as its uniform flow equivalent in eq.(22) apart from the bracketed term $\mathfrak{C}_n\bar{\theta})$. As before eq. (88) is validated by taking the limit as $\delta\to 0$. The bracketed term reduces to

$$\mathfrak{C}_n(\bar{\theta}) = \left[\mathrm{J}_{n-l}\,(\Delta_0 b) + \mathrm{H}^{(2)}_{n-l}\,(\Delta_0 b)\frac{\mathrm{J}'_n\,(\Delta_0 a_0)}{-\mathrm{H}^{(2)\prime}_n\,(\Delta_0 a_0)}\right], \tag{92}$$

which is the same as the bracketed term in eq.(22) showing that the linear profile expression reduces to the uniform flow expression.

IV. Convergence and Validation

The expressions derived in Sec. III.C are all in terms of a Fourier series. Therefore it is important to ensure the convergence of those series. Thus, following McAlpine at al. [8], the global relative error is introduced:

$$\epsilon \;=\; \sqrt{\frac{\frac{1}{M}\sum^{M}|p'_{N'}-p'_N|^2}{\frac{1}{M}\sum^{M}|p'_N|^2}}, \tag{93}$$

where, $p'_{N'}$ is the pressure calculated at the $(N+1)$th harmonic and p'_N is the pressure calculated at the Nth harmonic, and M is the number of grid points. When this error becomes sufficiently small, the series is considered to have converged. The key equations are eq.(79) and eq.(88). These are used to calculate the fuselage surface pressure and the far-field directivity — see examples of preliminary results in the next section. The convergence rate is dependent on

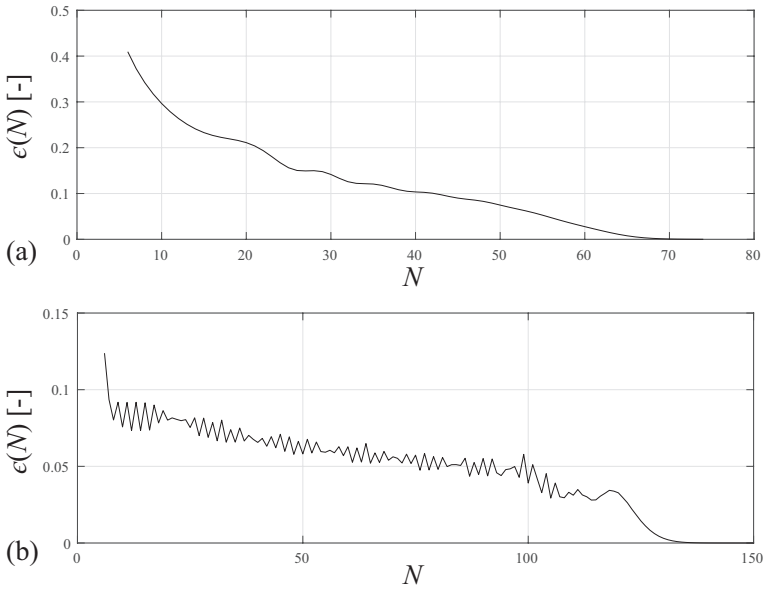

Fig. 6 Global relative error vs number of harmonics for [(a)] fuselage surface pressure expression (eq.(79)) at $k_0a = 20$, mode $(l, q) = (4, 1)$ and [(b)] far-field expression (eq.(88)) at $k_0a = 16$, mode $(l, q) = (10, 1)$. The other parameters are: $a = 0.5a_0$, $b = 3a_0$, $M_0 = 0.75$.

several parameters, the most important of which is frequency. The frequency is expressed in terms of a Helmholtz number, k_0a. In the examples shown in Fig. (6), convergence for the surface pressure takes about 70 harmonics at $k_0a = 20$. Lower frequencies require fewer harmonics. However, convergence for the far-field pressure takes in excess of 100 harmonics at $k_0a = 16$. Although more harmonics are required for the far-field pressure, evaluation of the far-field pressure does not require numerical calculation of the inverse Fourier z-transform, thus it is significantly faster to compute compared to the surface pressure despite requiring more harmonics to achieve convergence.

It is important to point out that where the series converges can be estimated asymptotically. It can be proven analytically that the dominant terms of the series for both expressions are the Bessel function terms in the bracketed terms $S_n(k_z, \omega_0)$ and $Y_l(\bar{\theta})$ respectively. Indeed, by taking the asymptotic form of the Bessel function when its order tends to infinity, the number of harmonics required for the series to converge can be determined. Furthermore, the Bessel function characteristically exhibits the behavior seen in Fig. (6(b)), namely highly oscillatory until it abruptly converges to zero at a sufficiently high order.

Furthermore, the expressions have been validated by taking the limit as $\delta \to 0$. As shown in Sec. III.C, the linear boundary layer expressions reduce to the uniform flow expressions when $\delta \to 0$, and that is reflected in the results obtained from the code as well. When the boundary layer thickness is reduced close to zero, the linear boundary layer code produces the same results as the code generated by McAlpine et al. [8] for uniform flow.

V. Preliminary Results

The purpose of this section is to present preliminary results that demonstrate the validity of the new expressions derived in this paper (eqs. (79) and (88)). Of particular interest is prediction of the level of boundary layer "shielding" caused by refraction of upstream sound propagation. Relevant results that quantify the shielding are compared with previous numerical results that can be found in Ref. [14].

The parameters used for the results presented in this section are given in Table 1. All geometrical characteristics are normalised based on a fuselage radius of unity ($a_0 = 1$). However, the frequency is expressed in terms of the non-dimensional Helmholtz number k_0a since the characteristic lengthscale for the fan tone source is the intake duct

radius a. A realistic Mach number at cruise condition is taken equal to 0.75, with the speed of sound estimated at cruising altitude of 30,000 ft. The dimensions, frequency and flow characteristics are chosen to be representative of a twin-engined aircraft for medium range flights.

Parameter	Value
a/a_0	0.5
$\bar{z}/a_0$	[-1,5]
b/a_0	3
β	0^o
M_0	0.75
(l, q)	$(4, 1)$

Table 1 Dimensions and flow characteristics for the results section.

In the modelling, the boundary-layer thickness δ on the fuselage surface is fixed. An estimate of the boundary layer thickness is obtained from the empirical model of a growing turbulent boundary layer on a flat plate, taking the boundary layer thickness at the source plane $\bar{z} = 0$. For a medium twin-engined aircraft, the boundary layer thickness at the source plane is roughly 5.5 % of the fuselage radius, i.e. $\delta = 0.055\, a_0$. The region of interest is upstream of the source ($\bar{z} > 0$), where boundary layer "shielding" is prominent owing to refraction of the upstream propagating sound that is radiated from the intake duct. Upstream of the source plane, the boundary layer is thinner, and predictions should be realistic for values of $\delta < 0.055\, a_0$. It is noted that since the theory developed in this paper does not include explicitly the duct, there is no diffraction around the intake lip, and downstream of the source ($\bar{z} < 0$) predictions of the surface pressure are not expected to be realistic.

Furthermore, the modelling utilises a linear boundary layer profile which is not a realistic profile shape. In this section, results calculated using the analytical method for a linear boundary layer are compared against previous numerical results for other profile shapes taken from Gaffney [14]. In order to be able to compare the two sets of results, an equivalency must be established between the linear boundary layer and other profile shapes that are used for comparison. This equivalency is achieved by equating the displacement thickness (δ^*) and the momentum thickness (ϑ) of the linear boundary layer with the displacement thickness and momentum thickness respectively of the boundary layer to compare against. Matching δ^* and ϑ yields appropriate values for M_w and δ for the equivalent linear boundary layer. This resulting linear boundary layer will have the same displacement and momentum thicknesses as the boundary layers to compare against, albeit the thickness of the different boundary layers will be different.

Predictions of the pressure are plotted in terms of the sound pressure level (SPL) in decibels (dB). The metric used to quantify the refraction effect upstream is the difference

$$\Delta_{bl} = \mathrm{SPL}_{bl} - \mathrm{SPL}, \tag{94}$$

where SPL_{bl} is the level that is predicted with the boundary layer, and SPL is the level that is predicted without the boundary layer. This quantity will highlight the areas where shielding occurs due to the presence of the boundary layer. Generally the near side of the cylindrical fuselage is of more interest because the highest levels are predicted adjacent to the source. Thus predictions are shown on the surface of the cylinder at $\bar{\phi} = 0^o$. On the other hand, on the far side of the cylindrical fuselage (around $\bar{\phi} = 180^o$) there is a shadow zone. It is difficult to evaluate the levels in the shadow zone region with a high degree of accuracy because the predicted levels can be in excess of 100 dB lower than the corresponding levels on the near side of the cylindrical fuselage. However, in reality there is no shadow zone since there are engines mounted on either side of the fuselage, thus accurate evaluation of very low levels in the shadow zone is not required for the practical application.

Figure (7) demonstrates the importance of the inclusion of the boundary layer. This result is calculated for a quarter-sine boundary layer profile. The upstream area ($\bar{z} > 0$) exhibits considerable shielding due to the presence of the boundary layer. Comparing the predicted results with the same boundary layer thickness, the shielding is greater when at the higher frequency. This is expected because at higher frequencies the ratio of the acoustic wavelength to the boundary layer thickness is lower, leading to a more prominent refraction effect. The comparison with the numerical results shows very good agreement for a thin boundary layer. That is expected because the validity of the asymptotic approach used by the analytic method relies on the boundary layer thickness to be sufficiently small. On the other hand,

for a very thick boundary layer, $\delta = 0.1a_0$, the asymptotic method is less accurate. The numerical predictions can reach shielding levels of -100 dB, and similar to predictions in the shadow zone, it is likely to be difficult to accurately calculate differences in levels in excess of 100 dB. Nevertheless, even for very thick boundary layers, the analytical method can still approximate the trend accurately.

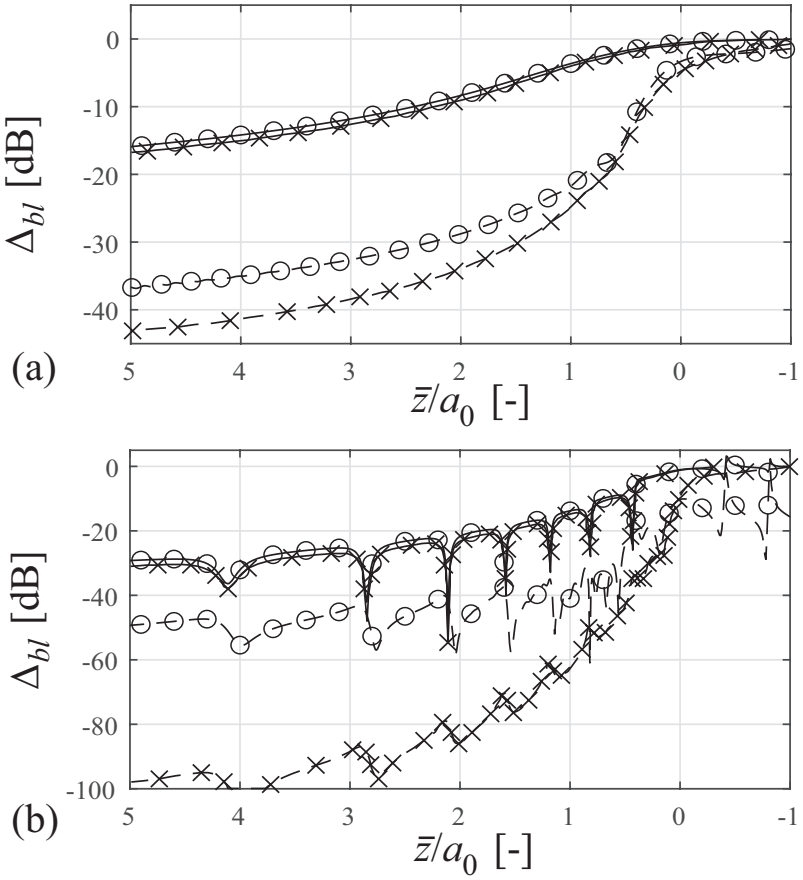

Fig. 7 Δ_{bl} **at** $\bar{\phi} = 0$ **for different boundary layer thicknesses. [(a)]** $k_0a = 5$ **and [(b)]** $k_0a = 20$**. Theoretical results produced with the asymptotic method are marked** (◯) **and numerical results are marked** (×) **for boundary layer thickness of** $\delta = 0.01a_0$ **(solid lines) and** $\delta = 0.1a_0$ **(dashed lines). The other parameters are:** $(l, q) = (4, 1)$**,** $a = 0.5a_0$**,** $b = 3a_0$**,** $M_0 = 0.75$ **and quarter-sine profile.**

The effect of the boundary layer thickness on the validity of the asymptotic approach is shown more clearly in Fig. (8). As expected, the agreement with the numerical result improves as the boundary layer thickness reduces. It is important to note that the results in Fig. (8) are for a high frequency. At lower frequencies the agreement between the theoretical and numerical results would be closer because the ratio of the acoustic wavelength to the boundary layer thickness is higher, resulting in effectively a thinner boundary layer.

The results in Figs. (7) and (8) are for a quarter-sine boundary layer profile. As previously explained, in order to approximate the quarter-sine profile, appropriate values of M_w and δ are determined for the linear profile by matching the displacement and momentum thicknesses. In fact for the quarter-sine profile, M_w is relatively small and δ for the linear profile is very similar to the thickness of the quarter-sine profile. On the other hand, in order to approximate a more realistic 1/7th power law profile that is commonly used to represent a turbulent boundary layer, the resulting equivalent linear profile has a large Mach number at the wall, $M_w = \frac{2}{3}M_0$, and a relatively small thickness, $\delta = 0.75\,\delta_{1/7}$, with subscript 1/7 denoting the 1/7th power law profile. Therefore to approximate a 1/7th power law profile, a thinner linear profile is required, which makes the asymptotic method even more accurate.

This is observed in Fig. (9), where for the example based on the power law profile the discrepancy between the theoretical results and the numerical results is very small. In fact it is also observed in Fig. (9) that the example of results

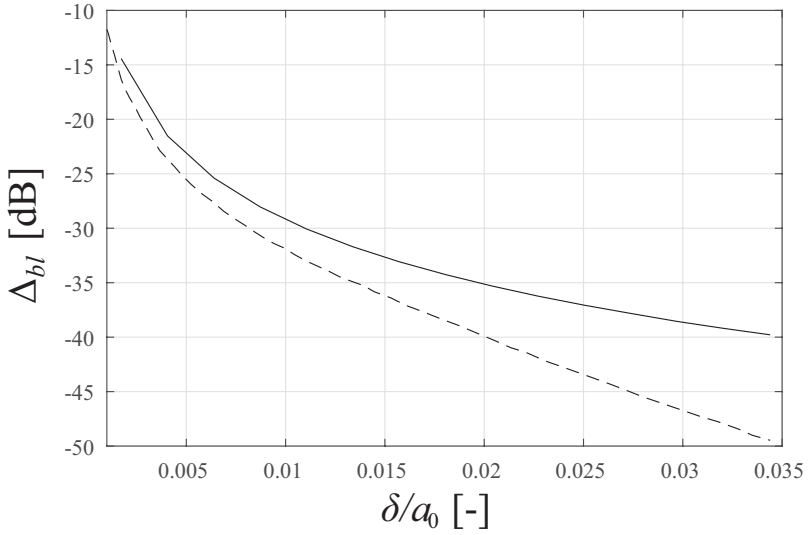

Fig. 8 Δ_{bl} **at** $\bar{\phi} = 0$ **and** $\bar{z} = 5a_0$ **vs boundary layer thickness. Comparison of theoretical results (solid line) and numerical results (dashed line). The other parameters are:** $(l, q) = (4, 1)$**,** $a = 0.5a_0$**,** $b = 3a_0$**,** $M_0 = 0.75$**,** $k_0 a = 20$ **and quarter-sine profile.**

for the linear profile only, comparing calculations with the theoretical and numerical method are not quite as close. This is because the boundary layer thickness used for the linear profiles in this example is thicker than the equivalent linear boundary layer that is used to compare against the 1/7th power law profile. It is therefore apparent that for sufficiently thin turbulent boundary layers, the new asymptotic approach which utilises an equivalent linear boundary layer profile produces very similar results to numerical calculations with a 1/7th power law profile. The asymptotic approach enables calculation of the theoretical results far more rapidly compared to the numerical approach.

Figures (10) and (11) are illustrative and show how the inclusion of the boundary layer affects the predictions of the acoustic field. The results are generated based on a 1/7th power law boundary layer that is representative of a realistic turbulent boundary layer on the fuselage. The far-field SPL polar directivity shown in Fig. (10) includes only the upstream region or polar angles up to 90^o. The azimuthal angle is $\bar{\phi} = 3\frac{\pi}{2}$ which corresponds to the upstream quadrant right underneath the flight path. Determination of the directivity pattern is essential for calculation of noise propagating towards the ground. In Fig. (10) it is observed that the inclusion of a boundary layer does not affect the predicted levels of the far-field pressure compared to the levels that are predicted with uniform flow. The major difference is the phase shift that can be observed regardless of the boundary layer thickness. Both thin and very thick boundary layers cause a significant phase shift upstream, significantly altering the levels at fixed polar angles.

The cylinder plots in Fig. (11) show SPL pressure contours on the cylindrical fuselage upstream of the source. Determination of the fuselage surface pressure is essential for calculation of cabin noise. For convenience, the levels shown in these plots have been normalised such that the maximum SPL is 0 dB. The boundary layer shielding effect caused by refraction of upstream sound propagation is seen in the cylinder plots, with greater shielding predicted as the thickness of the boundary layer becomes larger. Also, the shadow zone behind the cylinder tends to become wider with thicker boundary layers since more of the incident waves refract away from the surface.

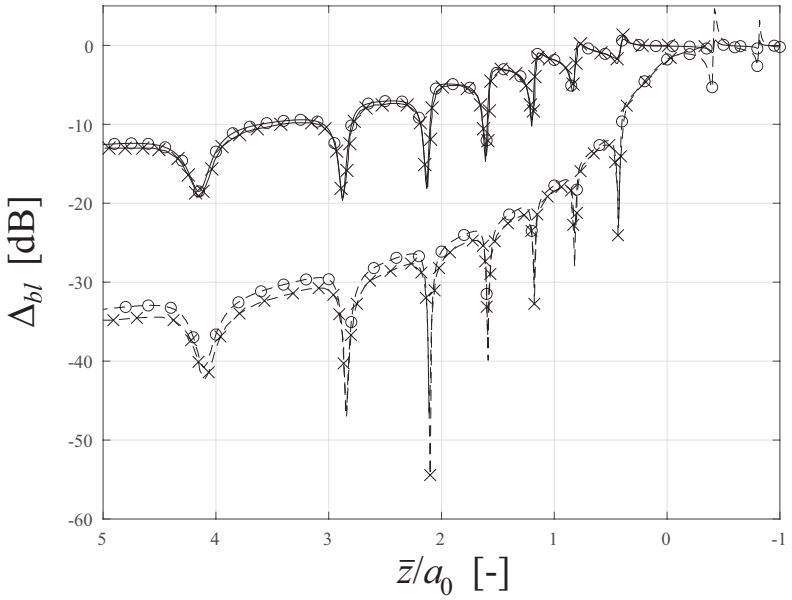

Fig. 9 Δ_{bl} **at** $\bar{\phi} = 0$ **for different velocity profiles. Theoretical results produced with the asymptotic method are marked (◯) and numerical results are marked (×) for 1/7th power law profile (solid lines) and linear profile (dashed lines). The other parameters are:** $(l, q) = (4, 1)$**,** $a = 0.5a_0$**,** $b = 3a_0$**,** $M_0 = 0.75$**,** $k_0 a = 20$ **and** $\delta = 0.01a_0$**.**

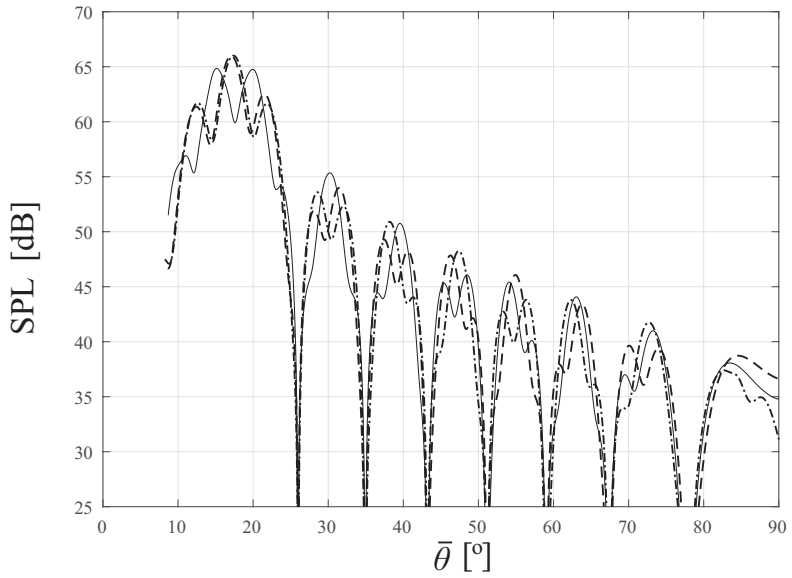

Fig. 10 Far-field polar directivity calculated from eq. (88). Comparison of results generated using the asymptotic method for $\delta = 0.01a_0$ **(dashed line) and** $\delta = 0.1a_0$ **(dashed-dotted line) and uniform flow (solid line). The other parameters are:** $k_0 a = 20$**,** $(l, q) = (4, 1)$**,** $a = 0.5a_0$**,** $b = 3a_0$**,** $M_0 = 0.75$ **and 1/7th power law profile.**

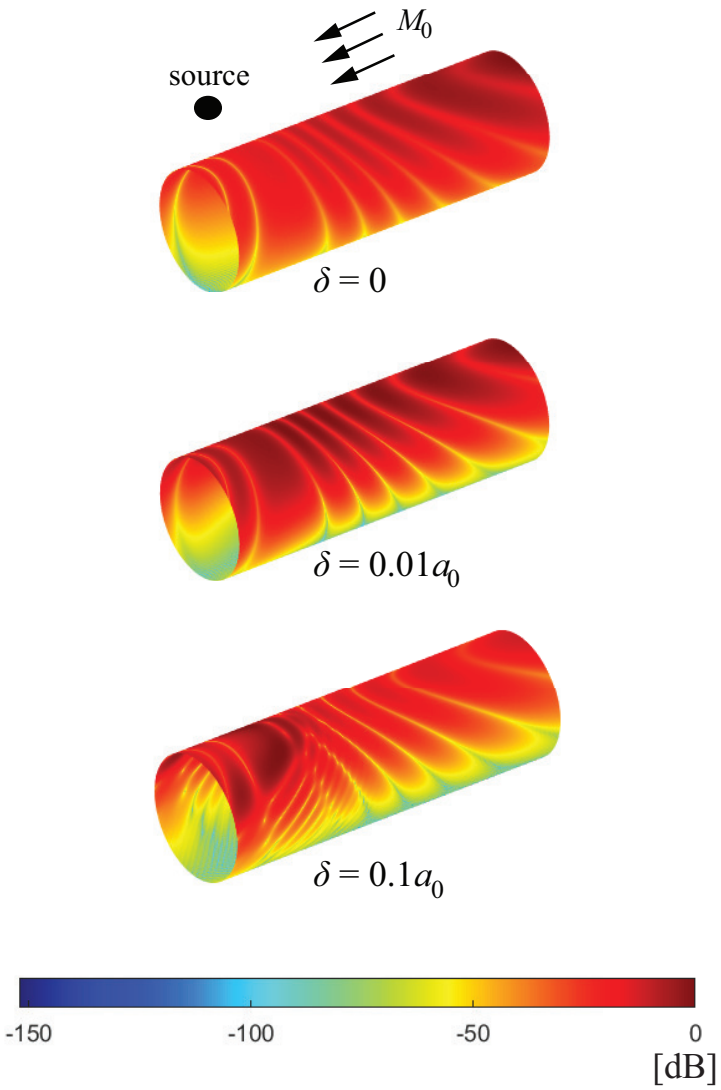

Fig. 11 SPL on the surface of the cylinder for uniform flow and two boundary layer thicknesses calculated from eq. (79). The other parameters are: $k_0 a = 20$**,** $(l, q) = (4, 1)$**,** $a = 0.5a_0$**,** $b = 3a_0$**,** $M_0 = 0.75$ **and 1/7th power law profile.**

VI. Conclusion

In this paper, the development of theoretical methods to predict scattering of fan tone noise from a turbofan engine by the airframe fuselage is reported. A new analytical approach is presented that can be used to predict the propagation of sound through the fuselage boundary layer, enabling predictions of boundary layer shielding caused by refraction of upstream sound propagation. Theoretical expressions for both the near and far-field acoustic pressure have been derived and validated. Comparisons with previous numerical results show that for thin boundary layers, the analytical method which uses an asymptotic approach can produce accurate results. Although the new method utilises a linear velocity profile, it proves to be very accurate at predicting the effect of a turbulent 1/7th power law profile even at relatively high frequency. Bearing in mind that typical average turbulent layer thicknesses are below 5% of the fuselage radius upstream of the source, the asymptotic method can be used to accurately model the scattering and refraction effect upstream of the source. Also, the advantage of the asymptotic approach is that numerical computation of the sound field in the boundary layer region is not required, providing a rapid engineering method to generate realistic results at very low computational cost.

The findings presented in this paper indicate that even simpler profiles could be used to approximate more realistic ones. A step-function velocity profile could be used that does not require any solution of the Pridmore-Brown equation, thus further simplifying the problem by removing any direct calculations with a shear velocity profile. However, the correct equivalency between the profiles would have to be investigated to ascertain whether matching the displacement and momentum thickness remains the optimal strategy to produce realistic results for the simpler problem. Furthermore, a potential issue that has not been tackled here is the critical layer as explained in Sec. III.C. This is currently under investigation, however Gaffney [14] concluded that the critical layer does not contribute significantly to prediction results for the range of parameters of interest in the turbofan application.

Appendix

A. Incident Field Derivation

As outlined by McAlpine and Kingan [9], the governing equation that describes the incident field due to the presence of a rotating monopole source q in uniform flow is the inhomogeneous convected wave equation,

$$\left(\nabla^2 - \frac{1}{c_0^2}\frac{\mathrm{D}^2}{\mathrm{D}t^2}\right)p' = -\rho_0\frac{\mathrm{D}q}{\mathrm{D}t}, \tag{95}$$

which written in full in cylindrical polar coordinates is,

$$\frac{\partial^2 p_i'}{\partial r^2} + \frac{1}{r}\frac{\partial p_i'}{\partial r} + \frac{1}{r^2}\frac{\partial^2 p_i'}{\partial \phi^2} + \frac{\partial^2 p_i'}{\partial z^2} - \frac{1}{c_0^2}\left(\frac{\partial}{\partial t} - U\frac{\partial}{\partial z}\right)^2 p_i' = -\rho_0\left(\frac{\partial}{\partial t} - U\frac{\partial}{\partial z}\right)q. \tag{96}$$

A single-frequency, rotating, monopole point source is considered with volume velocity

$$q(r,\phi,z,t) = Q_0 \mathrm{e}^{mi\omega_0 t}\frac{\delta(r-a)}{r}\left(\sum_{n=-\infty}^{\infty}\delta(\phi - \Omega t - 2\pi n)\right)\delta(z), \tag{97}$$

The three-dimensional delta function is used to describe the rotating monopole's radial and axial position (taken to be the duct's exit plane) and its periodicity around the source's centerline (or the duct's centerline). The monopole rotates around the centerline with angular velocity Ω. By taking the Fourier transform of eq. (96) the resulting equation can be solved using the method of variation of parameters. The full details of the solution are omitted for the sake of brevity. These details can be found in Ref. [9]. The Fourier transform involves Fourier transforms in z and t and the Fourier series in ϕ as follows:

$$\overline{p_{im}'}(r,k_z,\omega) = \int_{-\infty}^{\infty}\int_{-\pi}^{\pi}\int_{-\infty}^{\infty} p_i'(r,\phi,z,t)\mathrm{e}^{\mathrm{i}(k_z z + m\phi - \omega t)}\mathrm{d}z\mathrm{d}\phi\mathrm{d}t, \tag{98}$$

$$\Rightarrow p_i'(r,\phi,z,t) = \frac{1}{(2\pi)^3}\sum_{m=-\infty}^{\infty}\left(\int_{-\infty}^{\infty}\int_{-\infty}^{\infty}\overline{p_{im}'}(r,k_z,\omega)\mathrm{e}^{-\mathrm{i}(k_z z - \omega t)}\mathrm{d}k_z\mathrm{d}\omega\right)\mathrm{e}^{-\mathrm{i}m\phi}. \tag{99}$$

This transforms the derivatives as follows:

$$\frac{\partial}{\partial z} \rightarrow -\mathrm{i}k_z, \quad \frac{\partial}{\partial \phi} \rightarrow -\mathrm{i}m \quad \text{and} \quad \frac{\partial}{\partial t} \rightarrow \mathrm{i}\omega. \tag{100}$$

The Fourier transformed eq. (96) is

$$\frac{\mathrm{d}^2\overline{p'_{im}}}{\mathrm{d}r^2} + \frac{1}{r}\frac{\mathrm{d}\overline{p'_{im}}}{\mathrm{d}r} + \left\{\Gamma^2 - \frac{m^2}{r^2}\right\}\overline{p'_{im}} = Q_m, \tag{101}$$

where

$$Q_m = -\mathrm{i}Q_0\rho_0 c_0(k + k_z M_z)\frac{2\Omega(-1)^{m+1}\sin\pi(\frac{\omega-\omega_0}{\Omega})}{m\Omega - [\omega - \omega_0]}\frac{\delta(r-a)}{r}\sum_{n=-\infty}^{\infty}\delta(\omega - [\omega_0 + n\Omega]) \tag{102}$$

is the Fourier transformed right hand side of the equation with the radial wavenumber

$$\Gamma^2 = (k + k_z M)^2 - k_z^2. \tag{103}$$

The method of variation of parameters requires the solution to the homogeneous version of eq. (101) which is Bessel's differential equation. Since a radiation condition as $r \rightarrow \infty$ will be applied, it is more convenient to select $\mathrm{J}_m(\Gamma r)$ and $\mathrm{H}_m^{(2)}(\Gamma r)$ as the linearly independent solutions of Bessel's equation. Then, using the method of variation of parameters, the solution to eq. (101) is

$$\begin{aligned}\overline{p'_{im}} =& \mathrm{J}_m(\Gamma r)\left(A_m(k_z,\omega) - \mathrm{i}\frac{\pi}{2}\int_0^r Q_m(s)\mathrm{H}_m^{(2)}(\Gamma s)\, s\mathrm{d}s\right) + \\ & \mathrm{H}_m^{(2)}(\Gamma r)\left(B_m(k_z,\omega) + \mathrm{i}\frac{\pi}{2}\int_0^r Q_m(s)\mathrm{J}_m(\Gamma s)\, s\mathrm{d}s\right).\end{aligned} \tag{104}$$

Owing to the term $\frac{\delta(r-a)}{r}$ in Q_m (102), the solution is split into two domains, $r < a$ and $r > a$. The constants in eq. (104) can be found by applying the finiteness and radiation conditions. The Hankel function is singular as $r \rightarrow 0$, therefore it immediately follows from eq. (104) that $B_m = 0$. Furthermore, in order to have only outward propagating waves as $r \rightarrow \infty$, it can be shown that

$$A_m = \frac{\pi}{2}Q_0\rho_0 c_0(k + k_z M_z)\frac{2\Omega(-1)^{m+1}\sin\pi(\frac{\omega-\omega_0}{\Omega})}{m\Omega - [\omega - \omega_0]}\sum_{n=-\infty}^{\infty}\delta(\omega - [\omega_0 + n\Omega])\mathrm{H}_m^{(2)}(\Gamma a). \tag{105}$$

With A_m and B_m known, taking the inverse Fourier time-transform gives

$$\overline{p'_{im}}(r, k_z, t) = \frac{\pi}{2}Q_0\rho_0 c_0(k_{0m} + k_z M_z)\mathrm{H}_m^{(2)}(\Gamma_{0m} r_>)\mathrm{J}_m(\Gamma_{0m} r_<)\mathrm{e}^{\mathrm{i}(\omega_0 + m\Omega)t}, \tag{106}$$

where

$$r_> = \begin{cases} r, & r > a \\ a, & r < a \end{cases}; \tag{107}$$

$$r_< = \begin{cases} a, & r > a \\ r, & r < a \end{cases}, \tag{108}$$

and $k_{0m} = \frac{\omega_0 + m\Omega}{c_0}$ and $\Gamma_{0m}^2 = (k_{0m} + k_z M)^2 - k_z^2$.

B. Disc Source Derivation

This section briefly outlines the method used by McAlpine et al. [8]. For more details see Ref. [8]. The final incident field p'_i is the resulting field after integrating a distribution of monopoles over the cross section of the duct's termination. As outlined in Ref. [8] and shown in Fig. (12), consider an annular ring source with N monopoles distributed around a circle of radius η. Monopole s is located at $(r, \phi, z) = (\eta, s\Delta\psi, 0)$ where $\Delta\psi = 2\pi/N$ and $s = 0, 1, 2, \ldots, N-1$.

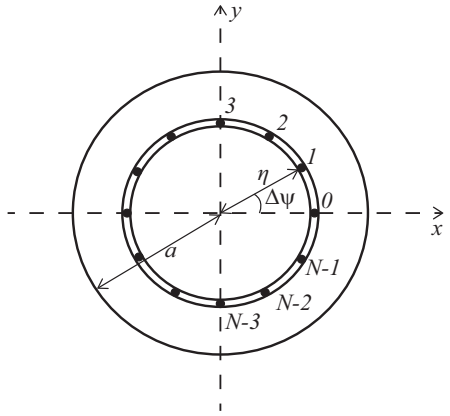

Fig. 12 Sketch of ring source. Taken from Ref. [8].

Equation (106) is the Fourier-transformed pressure field of a rotating monopole source derived by McAlpine and Kingan [8]. Therefore, by setting $\Omega = 0$ in eq. (106), and performing an inverse Fourier z-transform, the field owing to stationary monopole source $s = 0$ is recovered

$$p_i'^{(0)}(r, \phi, z, t) = \frac{1}{(2\pi)^2} \sum_{m=-\infty}^{\infty} \left(\int_{-\infty}^{\infty} \overline{p_{im}'^{(0)}}(r, k_z, t) \mathrm{e}^{-\mathrm{i}k_z z} \mathrm{d}k_z \right) \mathrm{e}^{-\mathrm{i}m\phi}, \tag{109}$$

where from eq. (106)

$$\overline{p_{im}'^{(0)}}(r, k_z, t) = \frac{\pi}{2} Q^{(0)} \rho_0 c_0 (k_0 + k_z M_z) \mathrm{H}_m^{(2)}(\Gamma_0 r_>) \mathrm{J}_m(\Gamma_0 r_<) \mathrm{e}^{\mathrm{i}\omega_0 t}, \tag{110}$$

and the variables are now defined as

$$r_> = \begin{cases} r, & r > \eta \\ \eta, & r < \eta \end{cases}; \tag{111}$$

$$r_< = \begin{cases} \eta, & r > \eta \\ r, & r < \eta \end{cases}. \tag{112}$$

It is important to note the radial wavenumber's behavior. With $\Omega = 0$, the wavenumber is defined as

$$\Gamma_0^2 = (k_0 + k_z M)^2 - k_z^2. \tag{113}$$

In order to ensure only outward propagating waves as $r \to \infty$, appropriate handling of Γ_0 is required. In the range

$$\frac{-k_0}{1 + M_z} < k_z < \frac{k_0}{1 - M_z} \tag{114}$$

Γ_0 is real and positive, whereas outside this range it will be imaginary $\Gamma_0 = -\mathrm{i}\gamma_0$ where $\gamma_0^2 = k_z^2 - (k_0 + k_z M)^2 > 0$.

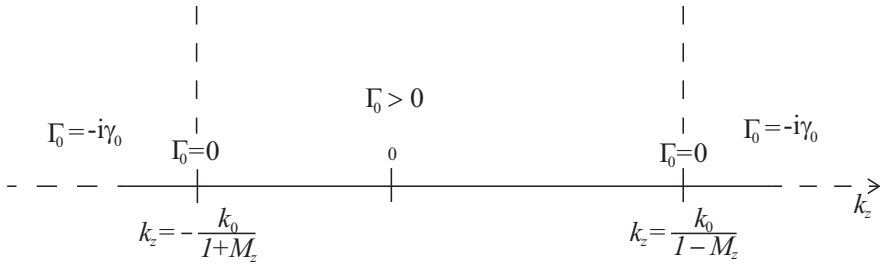

Fig. 13 Values of Γ_0 along the k_z-axis. Taken from Ref. [8].

As outlined in McAlpine at al. [8], the new angular coordinate $\widetilde{\phi}$ is introduced such that monopole s is located at $\widetilde{\phi} = 0$. This means that

$$\widetilde{\phi} = \phi - s\Delta\psi. \tag{115}$$

For every point source s on the ring, eqs. (109) and (110) apply, i.e.

$$p_i'^{(s)}(r,\phi,z,t) = \frac{1}{(2\pi)^2}\sum_{m=-\infty}^{\infty}\left(\int_{-\infty}^{\infty}\overline{p_{im}'^{(s)}}(r,k_z,t)\mathrm{e}^{-\mathrm{i}k_z z}\mathrm{d}k_z\right)\mathrm{e}^{-\mathrm{i}m\widetilde{\phi}}, \tag{116}$$

or

$$p_i'^{(s)}(r,\phi,z,t) = \frac{Q^{(s)}\rho_0 c_0}{8\pi}\sum_{m=-\infty}^{\infty}\left(\int_{-\infty}^{\infty}(k_0+k_z M_z)\mathrm{H}_m^{(2)}(\Gamma_0 r_>)\mathrm{J}_m(\Gamma_0 r_<)\mathrm{e}^{-\mathrm{i}k_z z}\mathrm{d}k_z\right)\mathrm{e}^{-\mathrm{i}m(\phi-s\Delta\psi)}\mathrm{e}^{\mathrm{i}\omega_0 t}. \tag{117}$$

In McAlpine et al. [8] each point source's strength $Q^{(s)}$ is calculated by using the axial particle velocity of the spinning mode (l,q) at position $(\eta, s\Delta\psi, 0)$,

$$Q^{(s)} = \frac{\xi_{lq}P_{lq}}{\rho_0 c_0}\mathrm{J}_l(\kappa_{lq}\eta)\mathrm{e}^{-\mathrm{i}ls\Delta\psi}\delta A, \tag{118}$$

where the elementary surface of the point source $\delta A = \eta\delta\eta\delta\psi$. The total incident field is

$$p_i'(r,\phi,z,t) = \sum_{s=0}^{N-1} p_i'^{(s)}(r,\phi,z,t), \tag{119}$$

which, by combining eqs. (109) and (118), and using the standard formula for a geometric progression, becomes

$$\begin{aligned} p_i'(r,\phi,z,t) =& N\frac{\xi_{lq}P_{lq}}{8\pi}\sum_{n=-\infty}^{\infty}\left(\int_{-\infty}^{\infty}(k_0+k_z M_z)\mathrm{H}_{l-nN}^{(2)}(\Gamma_0 r_>)\mathrm{J}_{l-nN}(\Gamma_0 r_<)\mathrm{J}_l(\kappa_{lq}\eta)\mathrm{e}^{-\mathrm{i}k_z z}\mathrm{d}k_z\right) \\ &\times \mathrm{e}^{\mathrm{i}nN\phi}\mathrm{e}^{-\mathrm{i}l\phi}\mathrm{e}^{\mathrm{i}\omega_0 t}\eta\delta\eta\delta\psi. \end{aligned} \tag{120}$$

The full details of the derivation of eq. (120) are in Ref. [8].

The distributed source is formed by taking the limit as the number of sources in the ring $N \to \infty$. This also means that $N\delta\psi \to 2\pi$, and only the $n = 0$ term is required. By integrating from $\eta = 0$ to a, the pressure for field points outside the duct $r > a$ is recovered:

$$p_i'(r,\phi,z,t) = \frac{\xi_{lq}P_{lq}}{4}\int_{-\infty}^{\infty}(k_0+k_z M_z)\Psi_{lq}\mathrm{H}_l^{(2)}(\Gamma_0 r)\mathrm{e}^{-\mathrm{i}k_z z}\mathrm{d}k_z\mathrm{e}^{-\mathrm{i}l\phi}\mathrm{e}^{\mathrm{i}\omega_0 t}, \tag{121}$$

where the function

$$\Psi_{lq} = \int_{\eta=0}^{a}\mathrm{J}_l(\Gamma_0\eta)\mathrm{J}_l(\kappa_{lq}\eta)\eta\mathrm{d}\eta, \tag{122}$$

can be evaluated exactly. For non-plane-wave excitation

$$\Psi_{lq} = \frac{\Gamma_0 a}{\kappa_{lq}^2 - \Gamma_0^2}\mathrm{J}_l(\kappa_{lq}a)\mathrm{J}_l'(\Gamma_0 a), \quad \Gamma_0 \neq \kappa_{lq}, \tag{123}$$

$$\Psi_{lq} = \frac{1}{2}\left(a^2 - \frac{l^2}{\kappa_{lq}^2}\right)\mathrm{J}_l^2(\kappa_{lq}a), \quad \Gamma_0 = \kappa_{lq}. \tag{124}$$

C. Graf's Addition Theorem

Graf's Addition Theorem is used to shift the coordinate system from the duct's centerline, (r, ϕ, z), to the adjacent cylinder's centerline, $(\bar{r}, \bar{\phi}, \bar{z})$. This must be done before the scattered field is introduced because the scattered field will be determined based on the cylinder's coordinate system.

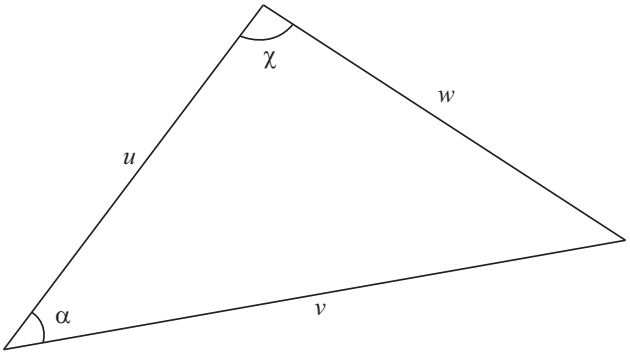

Fig. 14 Graf's Addition theorem.

From Abramowitz and Stegun [16], Graf's theorem is

$$\zeta_m(w)\mathrm{e}^{\mathrm{i}\chi} = \sum_{n=-\infty}^{\infty} \zeta_{m+n}(u)\mathrm{J}_n(v)\mathrm{e}^{\mathrm{i}n\alpha}, \tag{125}$$

where ζ_m can be any of the Bessel functions or linear combinations thereof. Also the condition $|u| > |ve^{\pm\mathrm{i}\alpha}|$ applies. The lengths w, u and v, and angles α and χ are part of the triangle shown in Fig. (14). Direct application of Graf's Theorem gives (triangle flipped taking $w = \Gamma_0 r$, $v = \Gamma_0 b$ and $u = \Gamma_0 \bar{r}$, while $\alpha = \bar{\phi} - \beta$ and $\chi = \phi - \bar{\phi}$)

$$\mathrm{H}_l^{(2)}(\Gamma_0 r)\,\mathrm{e}^{\mathrm{i}l\chi} = \sum_{n=-\infty}^{\infty} \mathrm{H}_{l+n}^{(2)}(\Gamma_0 \bar{r})\,\mathrm{J}_n(\Gamma_0 b)\,\mathrm{e}^{\mathrm{i}n\alpha}. \tag{126}$$

Note that by using the far-field assumption, $\bar{r} > b$, the theorem's condition, $|u| > |v|$, is satisfied. By rewriting $l \to -l$ and $n \to -n$

$$\mathrm{H}_{-l}^{(2)}(\Gamma_0 r)\,\mathrm{e}^{-\mathrm{i}l(\phi-\bar{\phi})} = \sum_{n=-\infty}^{\infty} \mathrm{H}_{-l-n}^{(2)}(\Gamma_0 \bar{r})\,\mathrm{J}_{-n}(\Gamma_0 b)\,\mathrm{e}^{-\mathrm{i}n(\bar{\phi}-\beta)}, \tag{127}$$

which becomes

$$\mathrm{H}_l^{(2)}(\Gamma_0 r)\,\mathrm{e}^{-\mathrm{i}l\phi} = \sum_{n=-\infty}^{\infty} \mathrm{H}_{l+n}^{(2)}(\Gamma_0 \bar{r})\,\mathrm{J}_n(\Gamma_0 b)\,\mathrm{e}^{-\mathrm{i}(l+n)\bar{\phi}}\,\mathrm{e}^{\mathrm{i}n\beta}. \tag{128}$$

Renaming $l + n = m$, so that $n = m - l$

$$\mathrm{H}_l^{(2)}(\Gamma_0 r)\,\mathrm{e}^{-\mathrm{i}l\phi} = \sum_{m=-\infty}^{\infty} \mathrm{H}_m^{(2)}(\Gamma_0 \bar{r})\,\mathrm{J}_{m-l}(\Gamma_0 b)\,\mathrm{e}^{-\mathrm{i}m\bar{\phi}}\,\mathrm{e}^{\mathrm{i}(m-l)\beta}, \tag{129}$$

with summation taken from $m = -\infty$ to ∞, since the integer l is treated as a constant.

Substitution into eq. (121) and renaming m by n gives

$$p_i'(\bar{r}, \bar{\phi}, \bar{z}, t) = \frac{1}{(2\pi)^2} \sum_{n=-\infty}^{\infty} \int_{-\infty}^{\infty} \overline{p_{in}'}(\bar{r}, k_z, t)\,\mathrm{e}^{-\mathrm{i}k_z\bar{z}}\,\mathrm{d}k_z\,\mathrm{e}^{-\mathrm{i}n\bar{\phi}}, \tag{130}$$

where

$$\overline{p_{in}'}(\bar{r}, k_z, t) = \pi^2 \xi_{lq} P_{lq}\,(k_0 + k_z M)\,\Psi_{lq}\,\mathrm{e}^{\mathrm{i}(n-l)\beta}\,\mathrm{J}_{n-l}(\Gamma_0 b)\,\mathrm{H}_n^{(2)}(\Gamma_0 \bar{r})\,\mathrm{e}^{\mathrm{i}\omega_0 t}. \tag{131}$$

On the other hand, by taking the near-field assumption $\bar{r} < b$ and flipping the triangle again (so that $u = \Gamma_0 b$, $v = \Gamma_0 \bar{r}$, $w = \Gamma_0 r$ and $\alpha = \bar{\phi} - \beta$, $\chi = \pi + \beta - \phi$) the incident field for the near-field is recovered:

$$\overline{p_{in}'}(\bar{r}, k_z, t) = \pi^2 \xi_{lq} P_{lq} (-1)^{l+n} (k_0 + k_z M)\,\Psi_{lq}\,\mathrm{e}^{-\mathrm{i}(l-n)\beta}\,\mathrm{H}_{l-n}^{(2)}(\Gamma_0 b)\,\mathrm{J}_n(\Gamma_0 \bar{r})\,\mathrm{e}^{\mathrm{i}\omega_0 t}. \tag{132}$$

D. Asymptotic Evaluation of the Far-Field Integral with the Method of Stationary Phase

In order to solve eq. (15), first the inverse Fourier z-transform must be determined

$$I_n \;=\; \frac{1}{2\pi}\int_{-\infty}^{\infty}\overline{p'_{tn}}\,(\bar{r},k_z,t)\;\mathrm{e}^{-\mathrm{i}k_z\bar{z}}\;\mathrm{d}k_z. \tag{133}$$

The integral can be evaluated by the method of stationary phase

$$I(x) \;=\; \int_a^b f(t)\mathrm{e}^{\mathrm{i}x\phi(t)}\mathrm{d}t, \quad \text{as } x\to\infty. \tag{134}$$

Then, if there is a single point $a\le c\le b$ such that $\phi'(c)=0$, provided that $\phi''(c)\neq 0$, then

$$I(x) \;\sim\; f(c)\left(\frac{2\pi}{x|\phi''(c)|}\right)^{1/2}\;\mathrm{e}^{\mathrm{i}x\phi(c)\pm\mathrm{i}\pi/4}, \quad \text{as } x\to\infty. \tag{135}$$

Since the aim is the evaluation of the far-field pressure, spherical polar coordinates are employed $(\bar{R},\bar{\theta},\bar{\phi})$. The integral is calculated in the limit as $\bar{R}\to\infty$. The substitutions are

$$\bar{r} \;=\; \bar{R}\sin\bar{\theta} \quad \text{and} \quad \bar{z} \;=\; \bar{R}\cos\bar{\theta}. \tag{136}$$

The dependence of the function $\overline{p'_{tn}}\,(\bar{r},k_z,t)$ on $\bar{r}$ is through the Hankel function which for large $\bar{R}$ can be replaced by its asymptotic form

$$\mathrm{H}_n^{(2)}\,(\Gamma_0\bar{r}) \;=\; \mathrm{H}_n^{(2)}\,(\Gamma_0\bar{R}\sin\bar{\theta}) \;\sim\; \sqrt{\frac{2}{\pi\Gamma_0\bar{R}\sin\bar{\theta}}}\,\mathrm{e}^{\frac{1}{2}n\pi\mathrm{i}}\,\mathrm{e}^{\frac{1}{4}\pi\mathrm{i}}\,\mathrm{e}^{-\mathrm{i}\Gamma_0\bar{R}\sin\bar{\theta}} \quad \text{as} \quad \bar{R}\to\infty. \tag{137}$$

Also, $\exp(-\mathrm{i}k_z\bar{z})\to\exp(-\mathrm{i}k_z\bar{R}\cos\bar{\theta})$ and the integral (134) can be expressed in the form

$$I_n \;\sim\; \frac{1}{2\pi}\int_{-\infty}^{\infty} f_n(k_z,\bar{R},\bar{\theta})\;\mathrm{e}^{-\mathrm{i}\bar{R}(\Gamma_0\sin\bar{\theta}+k_z\cos\bar{\theta})}\,\mathrm{d}k_z \quad \text{as} \quad \bar{R}\to\infty, \tag{138}$$

where

$$\begin{aligned} f_n(k_z,\bar{R},\bar{\theta}) \;&= \pi^2\xi_{lq}P_{lq}\,\mathrm{e}^{\mathrm{i}(n-l)\beta}\,(k_0+k_zM)\,\Psi_{lq}\sqrt{\frac{2}{\pi\Gamma_0\bar{R}\sin\bar{\theta}}}\,\mathrm{e}^{\frac{1}{2}n\pi\mathrm{i}}\,\mathrm{e}^{\frac{1}{4}\pi\mathrm{i}}\times \\ &\left[\frac{\mathrm{J}_{n-l}\,(\Gamma_0 b)\mathrm{H}_n^{(2)\prime}\,(\Gamma_0 a_0)-\mathrm{H}_{n-l}^{(2)}\,(\Gamma_0 b)\,\mathrm{J}'_n\,(\Gamma_0 a_0)}{\mathrm{H}_n^{(2)\prime}\,(\Gamma_0 a_0)}\right]\mathrm{e}^{\mathrm{i}\omega_0 t}. \end{aligned} \tag{139}$$

By introducing the similarity variables from Chapman [17],

$$\sigma^2 \;=\; 1-M^2, \tag{140}$$

$$\hat{R} \;=\; \frac{\bar{R}}{\sigma}(1-M^2\sin^2\bar{\theta})^{1/2}, \tag{141}$$

$$\cos\hat{\theta} \;=\; \frac{\cos\bar{\theta}}{(1-M^2\sin^2\bar{\theta})^{1/2}}, \tag{142}$$

$$\sin\hat{\theta} \;=\; \frac{\sigma\sin\bar{\theta}}{(1-M^2\sin^2\bar{\theta})^{1/2}}, \tag{143}$$

$$\tau \;=\; \sigma^2\frac{k_z}{k_0}-M, \tag{144}$$

$$\Gamma_0 \;=\; \frac{k_0}{\sigma}(1-\tau^2)^{1/2}, \tag{145}$$

$$k_z \;=\; \frac{k_0}{\sigma^2}(\tau + M), \tag{146}$$

$$\mathrm{d}k_z \;=\; \frac{k_0}{\sigma^2}\mathrm{d}\tau, \tag{147}$$

the integral I_n (138) is rewritten in the form

$$I_n \;\sim\; \frac{1}{2\pi}\int_{-\infty}^{\infty} g_m(k_z, \bar{R}, \bar{\theta})\, \mathrm{e}^{\mathrm{i}\bar{R}\hat{\phi}(\tau)}\, \mathrm{d}\tau \quad \text{as} \;\; \bar{R} \to \infty, \tag{148}$$

where

$$\hat{\phi}(\tau) \;=\; -\left(\frac{k_0}{\sigma}(1-\tau^2)^{1/2}\,\sin\hat{\theta} + \frac{k_0}{\sigma}(\tau + M)\,\cos\hat{\theta}\right), \tag{149}$$

and

$$\begin{aligned} g_n(\tau, \bar{R}, \bar{\theta}) \;&= \pi^2 \xi_{lq} P_{lq}\, \mathrm{e}^{\mathrm{i}(n-l)\beta}\left(k_0 + \frac{k_0}{\sigma^2}(\tau + M)M\right)\Psi_{lq}\left(\frac{k_0}{\sigma}(1-\tau^2)^{1/2}\right) \\ &\sqrt{\frac{2}{\pi\frac{k_0}{\sigma}(1-\tau^2)^{1/2}\hat{R}\sin\hat{\theta}}}\,\mathrm{e}^{\frac{1}{2}n\pi\mathrm{i}}\,\mathrm{e}^{\frac{1}{4}\pi\mathrm{i}}\,\mathrm{e}^{\mathrm{i}\omega_0 t}\,\frac{k_0}{\sigma^2}\times \\ &\left[\frac{\mathrm{J}_{n-l}\left(\frac{k_0}{\sigma}(1-\tau^2)^{1/2}b\right)\mathrm{H}_n^{(2)\prime}\left(\frac{k_0}{\sigma}(1-\tau^2)^{1/2}a_0\right) - \mathrm{H}_{n-l}^{(2)}\left(\frac{k_0}{\sigma}(1-\tau^2)^{1/2}b\right)\mathrm{J}_n'\left(\frac{k_0}{\sigma}(1-\tau^2)^{1/2}a_0\right)}{\mathrm{H}_n^{(2)\prime}\left(\frac{k_0}{\sigma}(1-\tau^2)^{1/2}a_0\right)}\right]. \end{aligned} \tag{150}$$

The equation $\phi'(c) = 0$ yields $c = \cos\hat{\theta}$. Also, when $|\tau| > 1$, Γ_0 becomes imaginary, so the integrand will become exponentially small as $\bar{R} \to \infty$. That means the limits of the integral can be replaced by $(-1, 1)$. With this substitution, the integral I_n (148) becomes

$$I_n \;=\; \frac{1}{2\pi}\, g_n(c)\left(\frac{2\pi}{\hat{R}|\hat{\phi}''(c)|}\right)^{1/2}\, \mathrm{e}^{\mathrm{i}\hat{R}\hat{\phi}(c)+\mathrm{i}\pi/4}, \quad \text{as}\;\; \hat{R} \to \infty. \tag{151}$$

where

$$\hat{\phi}(c) \;=\; -\frac{k_0}{\sigma}(1 + M\cos\hat{\theta}), \tag{152}$$

and

$$\hat{\phi}''(c) \;=\; \frac{k_0}{\sigma\sin^2\hat{\theta}}. \tag{153}$$

The final form of the integral I_n is given by

$$\begin{aligned} I_n \;&= \frac{1}{2\pi}\pi^2\xi_{lq}P_{lq}\,\mathrm{e}^{\mathrm{i}(n-l)\beta}\left(k_0 + \frac{k_0}{\sigma^2}(\cos\hat{\theta} + M)M\right)\Psi_{lq}\left(\frac{k_0}{\sigma}\sin\hat{\theta}\right)\sqrt{\frac{2}{\pi\frac{k_0}{\sigma}\hat{R}\sin^2\hat{\theta}}}\,\mathrm{e}^{\frac{1}{2}n\pi\mathrm{i}}\,\mathrm{e}^{\frac{1}{4}\pi\mathrm{i}}\times \\ &\mathrm{e}^{\mathrm{i}\omega_0 t}\,\frac{k_0}{\sigma^2}\left[\frac{\mathrm{J}_{n-l}\left(\frac{k_0}{\sigma}\sin\hat{\theta}b\right)\mathrm{H}_n^{(2)\prime}\left(\frac{k_0}{\sigma}\sin\hat{\theta}a_0\right) - \mathrm{H}_{n-l}^{(2)}\left(\frac{k_0}{\sigma}\sin\hat{\theta}b\right)\mathrm{J}_n'\left(\frac{k_0}{\sigma}\sin\hat{\theta}a_0\right)}{\mathrm{H}_n^{(2)\prime}\left(\frac{k_0}{\sigma}\sin\hat{\theta}a_0\right)}\right]\times \\ &\sqrt{\frac{2\pi}{\hat{R}\frac{k_0}{\sigma\sin^2\hat{\theta}}}}\,\mathrm{e}^{-\mathrm{i}\hat{R}\frac{k_0}{\sigma}(1+M\cos\hat{\theta})+\mathrm{i}\pi/4}, \end{aligned} \tag{154}$$

where $\Psi_{lq}(\frac{k_0}{\sigma}\sin\hat{\theta})$ is Ψ_{lq} (123) calculated taking $\Gamma_{0c} = \frac{k_0}{\sigma}\sin\hat{\theta}$. Then returning to the original coordinates using eqs. (141)-(147), and setting $\Delta_0 = \frac{k_0\sin\bar{\theta}}{(1-M^2\sin^2\bar{\theta})^{1/2}}$ and $S(\bar{\theta}) = \frac{((1-M^2\sin^2\bar{\theta})^{1/2}+M\cos\bar{\theta})}{\sigma^2}$ gives

$$\begin{aligned} I_n \;&= \frac{\mathrm{i}\pi\xi_{lq}P_{lq}k_0}{\bar{R}}\,\mathrm{e}^{\mathrm{i}(n-l)\beta}\,\frac{S(\bar{\theta})}{(1-M^2\sin^2\bar{\theta})}\,\Psi_{lq}(\Delta_0)\times \\ &\left[\frac{\mathrm{J}_{n-l}(\Delta_0 b)\mathrm{H}_n^{(2)\prime}(\Delta_0 a_0) - \mathrm{H}_{n-l}^{(2)}(\Delta_0 b)\,\mathrm{J}_n'(\Delta_0 a_0)}{\mathrm{H}_n^{(2)\prime}(\Delta_0 a_0)}\right]\mathrm{e}^{\frac{1}{2}n\pi\mathrm{i}}\,\mathrm{e}^{\mathrm{i}\omega_0 t}\,\mathrm{e}^{-\mathrm{i}k_0\bar{R}S(\bar{\theta})}. \end{aligned} \tag{155}$$

Finally, from eqs. (15) and (133)

$$p'_t\left(\bar{R},\bar{\theta},\bar{\phi},t\right) \;=\; \frac{1}{(2\pi)}\sum_{n=-\infty}^{\infty} I_n\,\mathrm{e}^{-\mathrm{i}n\bar{\phi}}, \tag{156}$$

or

$$\begin{aligned} p'_t\left(\bar{R},\bar{\theta},\bar{\phi},t\right) \;=\; & \frac{\mathrm{i}\xi_{lq}P_{lq}k_0}{2\bar{R}}\,\Psi_{lq}(\Delta_0)\,\frac{S(\bar{\theta})}{(1-M^2\sin^2\bar{\theta})}\sum_{n=-\infty}^{\infty}\mathrm{e}^{\mathrm{i}(n-l)\beta}\,\mathrm{e}^{\frac{1}{2}n\pi\mathrm{i}}\,\mathrm{e}^{\mathrm{i}\omega_0 t}\times \\ & \mathrm{e}^{-\mathrm{i}k_0\bar{R}S(\bar{\theta})}\,\mathrm{e}^{-\mathrm{i}n\bar{\phi}}\left[\frac{\mathrm{J}_{n-l}\left(\Delta_0 b\right)\mathrm{H}_n^{(2)\prime}\left(\Delta_0 a_0\right)-\mathrm{H}_{n-l}^{(2)}\left(\Delta_0 b\right)\mathrm{J}'_n\left(\Delta_0 a_0\right)}{\mathrm{H}_n^{(2)\prime}\left(\Delta_0 a_0\right)}\right]. \end{aligned} \tag{157}$$

Acknowledgments

The work in this article is part of the ARTEM project. This project has received funding from the European Union's Horizon 2020 research and innovation programme under grant No 769 350. ARTEM and other projects within the MG1-2-2017 call 'Reducing Aviation Noise' were initiated by the EREA 'Future Sky' initiative. The first author also acknowledges the financial contribution from the EPSRC via the University of Southampton's Doctoral Training Grant. The authors wish to acknowledge the technical input to this work from Christoph Richter (Rolls–Royce plc). Also the authors wish to acknowledge the continuing support provided by Rolls–Royce plc through the University Technology Centre in Propulsion Systems Noise at the Institute of Sound and Vibration Research.

References

[1] International Civil Aviation Organisation, "Volume 1: Aircraft noise", *Annex 16 to the Convention on International Civil Aviation: Environmental Protection*, 5th edition, 2008.

[2] Rolls–Royce, *The Jet Engine, 5th Edition*, Wiley Publications, Chichester, West Sussex, 2015.

[3] D.B. Hanson, "Shielding of prop-fan noise by the fuselage boundary layer", *Journal of Sound and Vibration*, **92**(4), pp. 591-598, 1984.

[4] D.B. Hanson and B. Magliozzi, "Propagation of propeller tone noise through a fuselage boundary layer", *Journal of Aircraft*, **22**(1), pp. 63-70, 1985.

[5] C.R. Fuller, "Free-field correction factor for spherical acoustic waves impinging on cylinders", *American Institute of Aeronautics and Astronautics Journal*, **27**(12), pp. 1722-1726, 1989.

[6] G.L. McAninch, "A note on propagation through a realistic boundary layer", *Journal of Sound and Vibration*, **88**(2), pp. 271-274, 1983.

[7] C.K.W. Tam and P.J. Morris, "The radiation of sound by the instability waves of a compressible plane turbulent shear layer", *Journal of Fluid Mechanics*, **98**(2), pp. 349-381, 1980.

[8] A. McAlpine, J. Gaffney, M.J. Kingan, "Near-field sound radiation of fan tones from an installed turbofan aero-engine", *Journal of Acoustical Society of America*, **138**(3), pp. 1313-1324, 2015.

[9] A. McAlpine and M.J. Kingan, "Far-field sound radiation due to an installed open rotor", *International Journal of Aeroacoustics*, **11**(2), pp. 213-245, 2012.

[10] J. Gaffney, A. McAlpine, M.J. Kingan, "Fuselage boundary-layer refraction of fan tones radiated from an installed turbofan aero-engine", *Journal of Acoustical Society of America*, **141**(3), pp. 1653-1663, 2017.

[11] H.Y. Lu, "Fuselage Boundary-Layer Effects on Sound Propagation and Scattering", *American Institute of Aeronautics and Astronautics Journal*, **28**(7), pp. 1180-1186, 1990.

[12] W. Eversman and R.J. Beckemeyer,"Transmission of sound in ducts with thin shear layers-Convergence to the uniform flow case", *Journal of the Acoustical Society of America*, **52**(1), pp. 216-220, 1972.

[13] D. C. Pridmore-Brown,"Sound propagation in a fluid flowing through an attenuating duct", *Journal of Fluid Mechanics*, **4**, pp. 393-406, 1958.

[14] J. Gaffney, *Theoretical Methods to Predict Near-field Fuselage Installation Effects due to Inlet Fan Tones*, Ph.D. thesis, University of Southampton, 2016.

[15] J.M. Tyler and T.G. Sofrin, "Axial flow compressor noise studies", *SAE Technical Paper*, **70**, pp. 309-332, 1962.

[16] M. Abramowitz and I. Stegun, *Handbook of Mathematical Functions*, Dover Publications, Inc., New York, 1965. (Chapter 9, pp. 363)

[17] C.J. Chapman, "Similarity variables for sound radiation in a uniform flow", *Journal of Sound and Vibration*, **233**, pp. 157-164, 2000.

[18] Bowman, J.J. Senior, T.B.A. and Uslenghi, P.L.E, *Electromagnetic and Acoustic Scattering by Simple Shapes*, North-Holland Publishing Co., 1969.

[19] S. Mariano,"Effect of wall shear layers on the sound attenuation in acoustically lined rectangular ducts", *Journal of Sound and Vibration*, **19**(3), pp. 261-275, 1971.

[20] S.-H. Ko,"Sound attenuation in acoustically lined circular ducts in the presence of uniform flow and shear flow", *Journal of Sound and Vibration*, **22**(2), pp. 193-210, 1972.